CrossMark

J. Fluid Mech. (2016), *vol.* 790, *pp.* 128–157. © Cambridge University Press 2016
doi:10.1017/jfm.2016.3

Inner–outer interactions of large-scale structures in turbulent channel flow

Jinyul Hwang[1], Jin Lee[1,2], Hyung Jin Sung[1,†] and Tamer A. Zaki[2]

[1]Department of Mechanical Engineering, KAIST, 291 Daehak-ro, Yuseong-gu, Daejeon 34141, Korea

[2]Department of Mechanical Engineering, Johns Hopkins University, Baltimore, MD 21218, USA

(Received 17 June 2015; revised 2 November 2015; accepted 2 January 2016;
first published online 2 February 2016)

Direct numerical simulation data of turbulent channel flow ($Re_\tau = 930$) are used to investigate the statistics of long motions of streamwise velocity fluctuations (u), and the interaction of these structures with the near-wall disturbances, which is facilitated by their associated large-scale circulations. In the log layer, the negative-u structures are organized into longer streamwise extent ($>3\delta$) in comparison to the positive-u counterparts. Near the wall, the footprint of negative-u structures is relatively narrow in comparison to the footprint of positive-u structures. This difference is due to the opposite spanwise motions in the vicinity of the footprints, which are either congregative or dispersive depending on the circulation of the outer roll cells. Conditional sampling of the footprints shows that the spanwise velocity fluctuations (w) are significantly enhanced by the dispersive motions of high-speed structures. On the other hand, the near-wall congregative motions of negative-u structures generate relatively weak w but intense negative-u regions due, in part, to the spanwise collective migration of near-wall streaks. The concentrated near-wall regions of negative-u upwell during the merging of the outer long scales – an effect that is demonstrated using statistical analysis of the merging process. This leads to a reduction of the convection speed of downstream negative-u structures and thus promotes the merging with upstream ones. These top-down and bottom-up interactions enhance the spatial coherence of long negative-u structures in the log region.

Key words: turbulence simulation, turbulent boundary layers, turbulent flows

1. Introduction

1.1. *Large-scale structures in wall-bounded turbulence*

In wall-bounded turbulent flows, large-scale structures in the outer layer contribute significantly to the transfer of momentum and to the turbulent kinetic energy. These motions possess both temporal and spatial coherence, which scales with the outer length scale δ, where δ is the channel half-height, the pipe radius, or the boundary layer thickness. Large-scale motions (LSMs) are the bulges in the outer region of turbulent boundary layers with a streamwise length of the order of 1–3δ (Adrian 2007). Adrian, Meinhart & Tomkins (2000) showed that LSMs are in the form of hierarchical structures of hairpin vortex packets, where the mature hairpin packets are associated

† Email address for correspondence: hjsung@kaist.ac.kr

https://doi.org/10.1017/jfm.2016.3 Published online by Cambridge University Press

with the bulges. The groups of vortices induce coherent induction and thus form relatively low-momentum zones. These structures contribute a significant fraction of the Reynolds shear stress in turbulent boundary layers (Ganapathisubramani, Longmire & Marusic 2003; Balakumar & Adrian 2007; Lee & Sung 2011) and internal flows (Liu, Adrian & Hanratty 2001; Guala, Hommema & Adrian 2006; Balakumar & Adrian 2007; Wu, Baltzer & Adrian 2012; Lee & Sung 2013; Ahn *et al.* 2015).

Structures with very long streamwise extent have received particular attention. Their spectral signature was detected in the premultiplied energy spectra of turbulent pipe flow by Kim & Adrian (1999). Those authors found two distinct peaks, one of which was at a wavelength significantly longer than the characteristic length of LSMs – they termed the associated structures 'very-large-scale motions' (VLSMs). Subsequently, experimental and numerical studies (e.g. del Álamo & Jiménez 2003; Guala *et al.* 2006; Balakumar & Adrian 2007; Hutchins & Marusic 2007*a*; Monty *et al.* 2007; Lee & Sung 2011, 2013; Wu *et al.* 2012) reported the presence of elongated turbulence structures $O(6\text{–}20\delta)$. Guala *et al.* (2006) defined VLSMs as streamwise wavelengths greater than 3δ, and computed their contributions to the streamwise turbulent energy and the Reynolds shear stress in pipe flows. Balakumar & Adrian (2007) extended this approach to turbulent boundary layers and channel flows in order to differentiate LSMs and VLSMs. Direct numerical simulation (DNS) of 30δ-long turbulent pipe flow ($Re_\tau = 685$) by Wu *et al.* (2012) showed a weak peak associated with VLSMs. They reported the distinct behaviour of LSMs and VLSMs in the net force spectra; the wavelength associated with LSMs decelerates the mean streamwise flow profile in the log layer while the VLSMs accelerate the flow even near the wall. Ahn *et al.* (2015) performed a DNS of a 30δ-long turbulent pipe flow at $Re_\tau = 3008$, and observed a bimodal distribution with a distinct outer peak that is related to VLSMs in the premultiplied energy spectra of the streamwise velocity fluctuations and the Reynolds shear stress.

1.2. *Near-wall influence of large-scale structures*

A robust feature of very long motions is their influence on the near-wall region. Using DNS data of turbulent channel flow at $Re_\tau = 934$, the footprint of very long low-speed motions was shown to extend to the wall and thus maintains the large scales in the near-wall region (Hutchins & Marusic 2007*a*). This near-wall impression contradicts scaling of the streamwise turbulence intensity using the friction velocity and the viscous length scale (del Álamo & Jiménez 2003; Hoyas & Jiménez 2006; Hutchins & Marusic 2007*a*), and underscores that the large scales and the near-wall region are interlinked. Furthermore, Hutchins & Marusic (2007*b*) demonstrated that the outer large scales modulate the small-scale energy in the near-wall region. Subsequently, Mathis, Hutchins & Marusic (2009) quantified this influence using the Hilbert transform. They defined the amplitude modulation coefficient using the correlation between the large-scale component of the streamwise fluctuating velocity (u) and the low-pass-filtered envelope of the small scales. The coefficient is positive in the near-wall region, which represents the top-down influence of outer large-scale structures on the near-wall region. In addition, the wall-normal and spanwise velocity fluctuations, as well as the instantaneous Reynolds shear stresses, associated with the small scales are all modulated in an analogous manner to that reported for the streamwise velocity perturbations (Talluru *et al.* 2014).

Baltzer, Adrian & Wu (2013) defined VLSMs as low-speed regions longer than 3δ in a DNS of pipe flow at $Re_\tau = 685$, which is consistent with earlier definitions

https://doi.org/10.1017/jfm.2016.3 Published online by Cambridge University Press

based on the streamwise wavelength (Guala *et al.* 2006; Balakumar & Adrian 2007; Wu *et al.* 2012). Very long meandering motions of low-speed fluid in the log layer contribute a large fraction of the Reynolds shear stress and of the streamwise kinetic energy in turbulent flows (Hutchins & Marusic 2007*a*; Monty *et al.* 2009). These structures were therefore the focus of a number of previous studies that noted the dominant contribution of the Q2 (ejection) events (e.g. Ganapathisubramani *et al.* 2003; Tomkins & Adrian 2003; Lee & Sung 2011; Baltzer *et al.* 2013). These low-speed motions are, however, flanked by high-speed regions (Hutchins & Marusic 2007*a*; Monty *et al.* 2007) which also contribute to the Reynolds shear stress through the Q4 (sweep) events. Dennis & Nickels (2011) evaluated the length and wall-normal extent of both the very-long low- and high-speed structures. The distribution of the latter was similar to that of low-speed streaks, but relatively shorter in streamwise extent. A similar trend was reported by Lee & Sung (2013) and Sillero, Jiménez & Moser (2014) who compared the streamwise and spanwise length scales of the high- and low-momentum regions. In addition, large-scale positive-u events amplify near-wall small-scale energy but the negative-u events attenuate the small-scale fluctuations (Hutchins & Marusic 2007*b*; Mathis *et al.* 2009; Ganapathisubramani *et al.* 2012). These observations suggest different near-wall influence of low- and high-speed regions associated with LSMs and VLSMs – the footprint effects that are explored in the present study.

1.3. *Organization of large-scale structures with outer roll cells*

Although the role of large-scale structures in wall-bounded turbulence can be quantified using conventional statistical measures, e.g. in terms of their contribution to the Reynolds stresses, their dynamics remain the subject of active research. Kim & Adrian (1999) conjectured that VLSMs are the concatenation of LSMs in the form of hairpin vortex packets. Using time-resolved instantaneous flow fields from DNS of a turbulent boundary layer ($Re_\tau = 850$), Lee & Sung (2011) presented evidence in support of that mechanism. In a later study, Baltzer *et al.* (2013) showed the concatenation of LSMs with extended streamwise alignment and along preferred azimuthal offset to form VLSMs in DNS of pipe flow ($Re_\tau = 685$). Alternative views include that VLSMs arise from a linear amplification mechanism (del Álamo & Jiménez 2006; McKeon & Sharma 2010), and that LSMs and VLSMs can self-sustain autonomously (Hwang & Cossu 2010). In this work, we focus on the genesis of VLSMs from the concatenation of LSMs. Recently, Lee *et al.* (2014) examined the spatial and temporal relationship between LSMs and VLSMs statistically. They found that the low-speed streaks with length 1–3δ in the outer region undergo merging. The merging process is facilitated by the difference in convection speed, which depends on the magnitude of the streamwise velocity fluctuations, u. The results by Lee *et al.* (2014) motivate a detailed analysis of the merging process starting from its precursors through its completion and its impact on the near-wall dynamics. The connection between the outer large scales and the near-wall motions was explored by Toh & Itano (2005) in the streamwise minimal channel at $Re_\tau = 349$. They reported that the large-scale outer structures are situated between a pair of large-scale circulations, and induce a collective aggregation of low-speed near-wall streaks. In turn, the intense near-wall motions reach up and can potentially have a bottom-up influence on the strength of outer velocity fluctuations (Adrian 2007). Based on evidence from several instantaneous cross-stream flow fields, Mito *et al.* (2007) pointed out the vortices in the log layer, which could lift fluid upwards and establish this bottom-up effect.

https://doi.org/10.1017/jfm.2016.3 Published online by Cambridge University Press

The presence of large-scale circulations, or roll cells, in the conditional averages of turbulent channel flow data ($Re_\tau = 934$) was also reported by Hutchins & Marusic (2007*b*). The conditional average based on the negative-u event showed the presence of a counter-rotating roll mode, and that the amplitude of small scales was strongly connected with the large-scale structures. Chung & McKeon (2010) also found a similar counter-rotating circulation on either side of the large-scale low-speed events in the conditionally averaged fields of large-eddy simulations of channel flow. They noted that the outer and near-wall regions of the flow are interlinked through the roll-cell patterns. The counter-rotating circulations were examined by Baltzer *et al.* (2013) who analysed turbulent pipe flow using conditional averaging and proper orthogonal decomposition. The roll-cell motions centred above the log layer were attributed to the preferred spanwise offset of LSMs that concatenated to form long low-momentum regions along a helical angle of 4°–8°. These earlier studies thus conjectured that the large-scale circulation in the outer region is associated with the large-scale structures as well as the intense near-wall velocity fluctuations which, in turn, potentially have a bottom-up influence on the outer dynamics – an interaction that is examined in detail in the present study.

The objective of the present study is to investigate the influence of low- and high-speed large-scale structures on the near-wall region by focusing on their associated large-scale circulations. We examine the induced dispersive or congregative near-wall motions, and the connection of this process to the formation of long low-speed structures in the log layer. Our approach relies on the analysis of data from DNS of turbulent channel flow at $Re_\tau = 930$ in a long computational domain of length $10\pi\delta$, which is sufficient for the study of very long structures. A brief description of the computational approach and the conditional sampling techniques for identifying the low- and high-speed instantaneous flow structures is provided in § 2. In § 3, the low- and high-speed structures are compared based on their spatial extent. Next, those structures associated with LSMs and VLSMs are examined using the conditional two-point correlations to reveal the spatial relationship with the surrounding velocity perturbations. We then perform conditional sampling of the footprints of wall-attached large-scale structures to see the impact on the near-wall region. The evolutions of near-wall and outer structures are reported based on instantaneous flow fields, with particular focus on their interaction, which facilitates merging of the large outer scales. Finally, a summary of the main findings is provided in § 4.

2. Numerical details

2.1. *Direct numerical simulation*

The Navier–Stokes equations for incompressible flow are solved using the fully implicit decoupling method by Kim, Baek & Sung (2002). The configuration corresponds to fully developed turbulent channel flow, and details of the DNS and the validation are provided in the earlier study by Lee *et al.* (2014). In the present study, x, y and z denote the streamwise, wall-normal and spanwise directions, respectively, and the associated components of velocity fluctuations are u, v and w; capital letters are used to indicate mean quantities. An angle bracket $\langle\cdot\rangle$ denotes ensemble averaging. The superscript $+$ represents quantities normalized by the viscous scales, namely the friction velocity, u_τ, and viscosity, ν. The Reynolds number based on the channel half-height, δ, and the laminar centreline velocity, U_{CL}, is $Re_\delta = 28\,000$, and the friction Reynolds number is $Re_\tau = 930$. The domain size in the streamwise and spanwise directions is $(L_x, L_z) = (10\pi\delta, 3\pi\delta)$. A staggered mesh is employed with

https://doi.org/10.1017/jfm.2016.3 Published online by Cambridge University Press

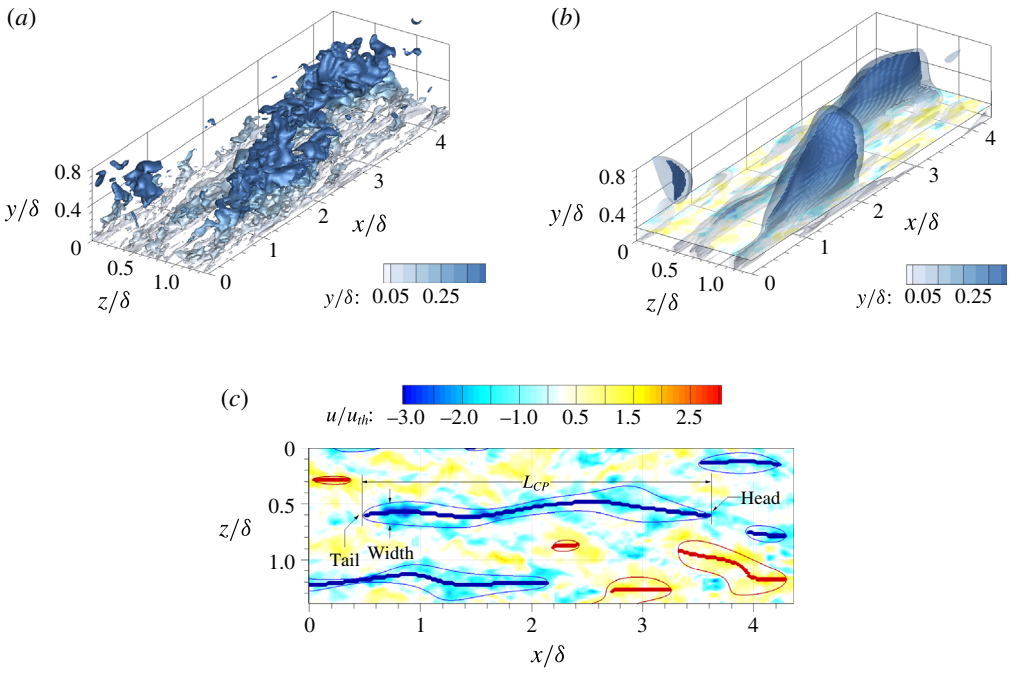


FIGURE 1. (Colour online) Isosurfaces of (*a*) the negative streamwise velocity fluctuations ($u=-u_{th,raw}$) and (*b*) the Gaussian and long-wavelength-pass-filtered flow field ($\hat{u}=-u_{th}$) with the characteristic projections (*CP*). (*c*) The wall-parallel plane $y/\delta=0.15$ at the same instance as frame (*b*); the thick and thin blue (red) lines represent the $CP=-1$ ($CP=+1$) and $\hat{u}=-u_{th}$ ($\hat{u}=+u_{th}$), respectively.

$4993\times401\times2497$ grid points in the x, y and z directions, respectively. The grid sizes in the homogeneous directions are $\Delta x^+=5.86$ and $\Delta z^+=3.51$. The minimum and maximum wall-normal grid spacings are $\Delta y^+_{min}=0.0287$ and $\Delta y^+_{max}=7.31$, respectively. The simulation is performed at a constant mass flow rate, and the time step is $\Delta t=0.002\delta/U_{CL}$, or $\Delta t^+=0.0618$, and the averaging period spans $220\delta/U_{CL}$, corresponding to seven sweeps across the flow domain. A total of 2010 snapshots are stored, with each two consecutive fields separated by $0.1\delta/U_{CL}$ (or $\Delta t^+=3.09$). In the present study, the following wall-normal regions are defined: the near-wall region $y^+<30$; the log layer $30<y^+<0.15\delta^+$; and the channel core $y^+>0.15\delta^+$.

2.2. *Structure-detection method*

To investigate the formation of elongated u structures in space and time, streak detection and conditional sampling techniques are applied to the instantaneous fields. The streak-detection algorithm is based on the work by Nolan & Zaki (2013), where local extrema of u are used to reconstruct the three-dimensional (3D) streamwise-elongated structures. Further detailed descriptions of the methodology can be found in Zaki (2013). Figure 1 displays an example of the outcome of the detection method. The threshold $u_{th,raw}=0.1U_b$, where U_b is the bulk velocity, is used in the present study (Dennis & Nickels 2011; Baltzer *et al.* 2013; Lee *et al.* 2014). The procedure is outlined below.

https://doi.org/10.1017/jfm.2016.3 Published online by Cambridge University Press

Step 1: *Gaussian filter*. A two-dimensional Gaussian filter is applied in the y–z plane to the instantaneous u field. The standard deviation (σ) of the Gaussian filter is determined as a function of the wall-normal distance, because the spanwise length scale of the u motions varies with height from the wall. The standard deviation is set to the half-width of the spanwise two-point correlation of u at a level of 0.5. This choice prevents adjacent negative u from counterbalancing the positive u, and *vice versa*. The curve-fitted standard deviation function $\sigma(y/\delta)$ is

$$\sigma/\delta = 0.1513(y/\delta)^3 - 0.5142(y/\delta)^2 + 0.4992(y/\delta) + 0.0176. \tag{2.1}$$

Step 2: *Long-wavelength-pass filter*. A long-wavelength-pass filter is applied to the Gaussian-filtered flow fields in order to isolate structures longer than 1δ in the streamwise direction. If the streamwise filter is applied alone, it leads to discontinuous isosurfaces of the velocity field, which are not suitable for identifying contiguous u structures along the streamwise direction (Lee *et al.* 2014). Hence, the Gaussian filter is also needed in order to ensure that the u isosurfaces are smooth.

The smoothed isosurfaces in figure 1(*b*) illustrate the filtered flow field, $\hat{u}$. Owing to the weakened magnitude of u by the filters, the velocity threshold is corrected, $u_{th}(y) = f(y)u_{th,raw}$, where $f(y) = \langle u(\boldsymbol{x})\hat{u}(\boldsymbol{x})\rangle / \langle u(\boldsymbol{x})u(\boldsymbol{x})\rangle$. Then local extrema are identified in the filtered fields along lines in the spanwise direction. Note that $\hat{u}$ is a smooth function due to the Gaussian filter and, as a result, the computed local extrema at the core of each flow structure are contiguous (see figure 14 in Lee *et al.* (2014)). Neighbouring extrema thus mark the cores of the velocity disturbances. The extrema that are connected in the streamwise direction are linked and labelled as a unique object, which can be regarded as the characteristic projections (*CP*) of the flow structures. In this manner, *CP* represents the streamwise and wall-normal extents of LSMs:

$$CP(x, y, z) = \begin{cases} +1 & \text{where } \partial\hat{u}/\partial z = 0 \text{ and } \hat{u} > u_{th}, \\ -1 & \text{where } \partial\hat{u}/\partial z = 0 \text{ and } \hat{u} < -u_{th}, \\ 0 & \text{otherwise.} \end{cases} \tag{2.2}$$

Based on the above definition, $CP = +1$ marks high-speed structures and $CP = -1$ identifies low-speed ones. Figure 1(*b*) shows a transparent isosurface of the filtered velocity field, along with the surface $CP = -1$ coloured by wall-normal height. Figure 1(*c*) shows a top view of the u-perturbation contours at $y/\delta = 0.15$. The thick solid lines show the intersection of the wall-parallel plane with the *CP* surface and they mark the streamwise and spanwise positions of the organized motion. The most downstream and upstream ends of *CP* denote the head and the tail of the streak, respectively. The streamwise length, L_{CP}, of each streak is measured and the spanwise boundary of the streak is defined by identifying lower and upper bounds ($\hat{u} = \pm u_{th}$) on either side of the streak core (see figure 1*c*). If there are multiple adjacent streaks (for example, near $x/\delta = 4$–6 in figure 3*b*), the boundaries of each streak are adjusted to the spanwise location where $\partial\hat{u}/\partial z$ changes sign.

3. Results and discussion

3.1. *Long streaks of streamwise velocity fluctuations*

In this section, the length and area of long negative- and positive-u regions are examined using the structure-detection algorithm (§ 2.2). Figure 2 shows the

https://doi.org/10.1017/jfm.2016.3 Published online by Cambridge University Press

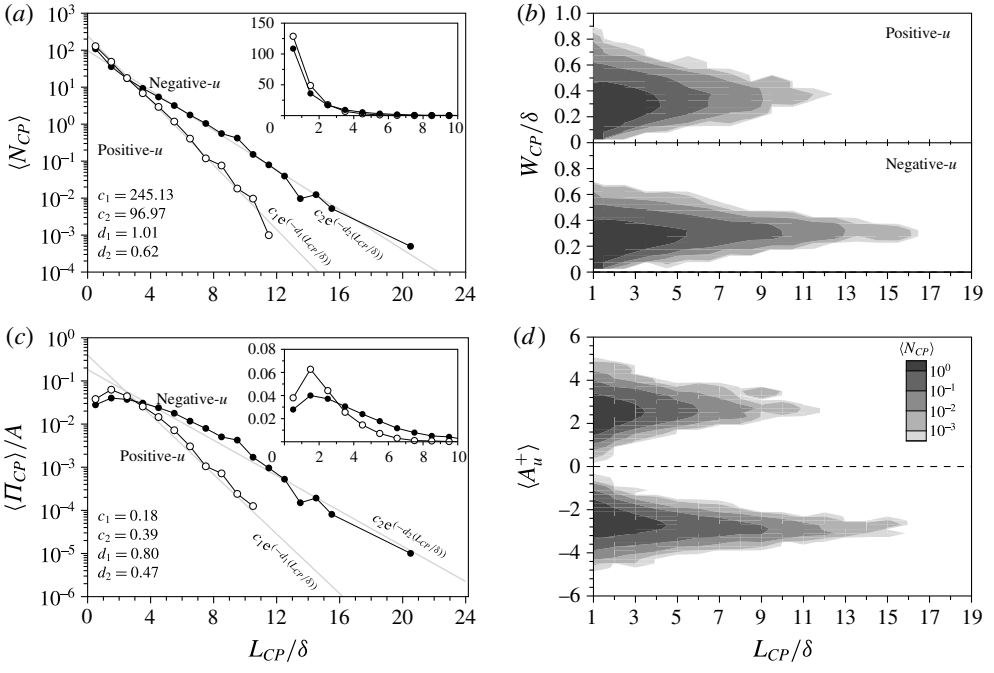


FIGURE 2. Histograms of the streamwise length (L_{CP}) of low- and high-speed streaks at $y/\delta = 0.15$. (*a*) The mean number of the streaks per field ($\langle N_{CP} \rangle$) in the wall-parallel plane. (*b*) The spanwise width (W_{CP}) of low- and high-speed streaks. (*c*) The mean area occupied by the structures per field ($\langle \Pi_{CP} \rangle$) versus their streamwise length; $\langle \Pi_{CP} \rangle$ is normalized by the total area of the wall-parallel plane ($A = L_x \times L_z$). (*d*) The mean amplitude (A_u) of the low- and high-speed streaks of a particular length. In (*a*,*c*), the closed and open symbols represent low- and high-speed streaks, respectively. The grey lines mark an exponential curve fit, and the insets show the results in linear scale. In (*b*,*d*), the contour lines indicate $\langle N_{CP} \rangle$. The bin size for L_{CP} is 1δ.

populations of negative- and positive-u structures versus their streamwise length, L_{CP}, at $y/\delta = 0.15$. The mean number ($\langle N_{CP} \rangle$) of negative-u (closed symbol) and positive-u (open symbol) regions is displayed in figure 2(*a*). A single occurrence, $\langle N_{CP} \rangle = 1$, means that an average of one structure with the specified length is observed in this wall-parallel plane per unit time. Structures that are recorded more than once per field have a streamwise length less than 8δ for the negative-u regions and 6δ for the positive counterparts. The vast majority of detected streaks have a streamwise length less than 1δ. The maximum streamwise extent of negative-u regions is approximately 20δ, while that of positive structures is only 12δ. Although the populations of both negative- and positive-u regions decrease logarithmically with their length, the negative-u regions tend to be longer than their positive counterparts and the latter are relatively biased towards shorter lengths. Beyond 3δ in particular, the disparity between the populations of low and high speed becomes more pronounced. The slope of the populations, d_i, is found to be steeper for positive-u regions, where $d_1 = 1.01$ and $d_2 = 0.62$ for positive and negative u, respectively. The results based on the present detection algorithm are in agreement with those by Dennis & Nickels (2011) and by Baltzer *et al.* (2013) despite the difference in the structure identification procedure. Dennis & Nickels (2011) counted both low- and high-speed structures

https://doi.org/10.1017/jfm.2016.3 Published online by Cambridge University Press

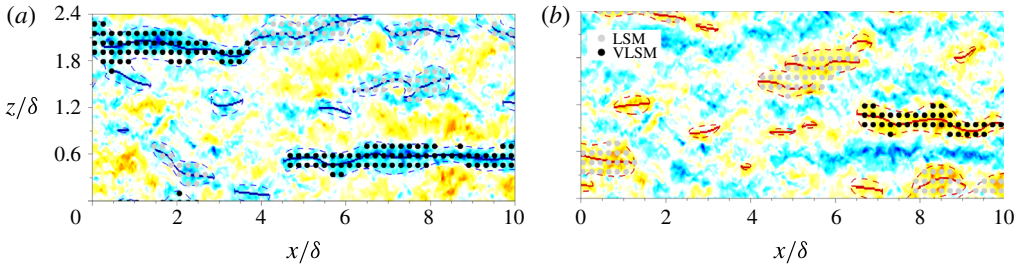


FIGURE 3. (Colour online) Area identification at $y/\delta = 0.15$: (*a*) nLSM (u_1) and nVLSM (u_2); (*b*) pLSM (u_3) and pVLSM (u_4); here n = negative and p = positive. The contour levels are the same as in figure 1(*c*). The solid and dashed lines represent $CP = \pm 1$ and $\hat{u} = \pm u_{th}$, respectively.

whose streamwise lengths were greater than 2δ in a turbulent boundary layer. For low-speed structures, 44 % of the structures were below 3δ while 54 % of the high-speed structures were in the same range. The distributions evaluated using the present algorithm show similar trends: 43 % and 60 % for low- and high-speed regions, respectively. The predicted ratio of long low- and high-speed structures ($>2\delta$) are also similar in the two studies, approximately 1.3–1.5. Low-speed regions that are longer than 7δ are less than 5 % of the total population, consistent with Baltzer *et al.* (2013).

The population trends of the positive- and negative-u regions classified based on their streamwise length (L_{CP}) and spanwise width (W_{CP}) are displayed in figure 2(*b*). The width of each region is computed by measuring lower and upper bounds along $CP = \pm 1$ (see figure 1),

$$W_{CP}(L_{CP}) = \frac{1}{L_{CP}} \int_{z_1}^{z_2} \int_{tail}^{head} \zeta(x, z; L_{CP})\, \mathrm{d}x\, \mathrm{d}z, \tag{3.1}$$

where z_1 and z_2 are lower and upper bounds along $CP = \pm 1$ and

$$\zeta(x, z; L_{CP}) = \begin{cases} 1, & \text{if } |\hat{u}| > u_{th}, \\ 0, & \text{otherwise.} \end{cases} \tag{3.2}$$

The contour lines represent $\langle N_{CP} \rangle$ and only streaks with length greater than 1δ are shown. As the length of the streaks increases, the streaks maintain their spanwise width around 0.3δ. While the most probable width of positive- and negative-u streaks remains comparable, $W_{CP} \approx 0.3\delta$, the maximum width of negative-u streaks is generally narrower than its positive-u counterpart. The width of short positive-u streaks ($<3\delta$) reaches up to 0.8δ. In general, the positive-u streaks are shorter and wider than the negative-u ones. To analyse the spatial extent occupied by the positive- and negative-u structures, figure 2(*c*) shows the mean area $\langle \Pi_{CP} \rangle$ of the streaks in the $y/\delta = 0.15$ plane. The area occupied by streaks of a particular length $\Pi_{CP}(L_{CP})$ is defined as

$$\Pi_{CP}(L_{CP}) = \sum_{i=1}^{N_{CP}} A_i(L_{CP}), \tag{3.3}$$

https://doi.org/10.1017/jfm.2016.3 Published online by Cambridge University Press

where A_i is the area for each streak,

$$A_i(L_{CP}) = \int_{z_1}^{z_2} \int_{tail}^{head} \zeta(x, z; L_{CP})\, \mathrm{d}x\, \mathrm{d}z. \tag{3.4}$$

The area Π_{CP} is normalized by the total area of the wall-parallel plane ($A = L_x \times L_z$). The sum of Π_{CP} indicates the total area fraction occupied by streamwise velocity fluctuations greater than the threshold value. The area fraction of the weak region, where the perturbation field is weaker than the threshold value, is not included here. The total area fractions of the negative and positive u are similar in the log layer, 21 % and 19 %, respectively, although the area fractions depend on the streamwise length of the structures. Each short-length streak has a smaller area compared to the longer streaks while Π_{CP} for short-length structures is greater than the longer structures due to the higher number density in the flow field. The area fraction has a peak between 1δ and 3δ. In addition, the area fraction of the positive-u regions crosses the negative counterpart around $L_{CP} = 3\delta$, similar to the trend of their respective populations reported in figure 2(*a*). Owing to the smaller population of the positive-u regions ($>3\delta$), their area fraction rapidly drops in comparison to the negative-u structures. The slopes of the area fraction are $d_1 = 0.80$ and $d_2 = 0.47$ for positive and negative u, respectively. Moreover, the area fraction of the negative-u regions with lengths longer than 3δ is approximately 10 % (11 % for $L_{CP} < 3\delta$) and of the positive counterparts is 5 % (14.5 % for $L_{CP} < 3\delta$). Although the population of long negative-u structures is small (logarithmic decrease in their population in figure 2*a*), they occupy a similar area fraction as the shorter structures. On the other hand, the area of the positive-u regions is mainly occupied by the relatively short structures ($L_{CP} < 3\delta$) at $y/\delta = 0.15$. It should be noted that the effect of the threshold u_{th} employed in our structure identification was examined (see Appendix). We found that the general trends reported in this section remain qualitatively unchanged.

To compare the magnitude of the streamwise velocity fluctuations within the organized motions, the strength of the streamwise streaks was evaluated along L_{CP}. The mean amplitude for each streak, A_u, is

$$A_u(L_{CP}, y) = \frac{1}{L_{CP}} \int_{tail}^{head} u|_{CP=\pm 1}\, \mathrm{d}x. \tag{3.5}$$

The distributions of $A_u(L_{CP}, y^+ = 0.15\delta^+)$ are shown in figure 2(*d*). The contours at $A_u > 0$ illustrate the distribution of the positive-u streaks and those of the negative-u streaks are shown as $A_u < 0$. Both distributions are relatively wider for the shorter length and become narrower as the length of the streaks increases. Although the distributions of the streak amplitudes are similar for both negative and positive u, the long streaks ($\geqslant 12\delta$) are only observed in negative u. In addition, these long streaks carry significantly higher disturbance amplitude ($|A_u^+| \approx 3$) compared with $u_{rms}^+ = 1.87$ at $y/\delta = 0.15$. Their long streamwise extent indicates that the very long-u regions contribute a significant fraction of the Reynolds stresses.

The VLSMs are motions whose streamwise wavelengths are greater than 3δ (Guala *et al.* 2006; Balakumar & Adrian 2007; Wu *et al.* 2012). Several studies have therefore used the energy contained within this wavelength range to differentiate LSMs and VLSMs (Dennis & Nickels 2011; Baltzer *et al.* 2013; Lee *et al.* 2014; Lee, Ahn & Sung 2015). In particular, Baltzer *et al.* (2013) defined the VLSMs as the negative-u streaks longer than 3δ at $y/\delta = 0.15$, and their contribution to the

https://doi.org/10.1017/jfm.2016.3 Published online by Cambridge University Press

Reynolds shear stress at that wall-normal position was computed by Lee & Sung (2011, 2013). In the present study, streamwise-extended regions of contiguous *CP* in the x–z plane ($y/\delta = 0.15$) were classified into LSM and VLSM using a 3δ limit, and these motions were further differentiated according to their sign (n = negative and p = positive). This classification yields the following four categories (Lee *et al.* 2015): nLSM ($1\delta \leqslant L_{CP}|_{CP=-1} < 3\delta$); nVLSM ($L_{CP}|_{CP=-1} \geqslant 3\delta$); pLSM ($1\delta \leqslant L_{CP}|_{CP=+1} < 3\delta$); and pVLSM ($L_{CP}|_{CP=+1} \geqslant 3\delta$). Figure 3 shows an example of these u structures. For convenience, we introduce an area indicator $I(x, z)$, which represents the bounded area of each motion based on its sign and length:

$$I(x,z) = \begin{cases} 1 & \text{where } \zeta(x,z;L_{CP})|_{nLSM} = 1, \\ 2 & \text{where } \zeta(x,z;L_{CP})|_{nVLSM} = 1, \\ 3 & \text{where } \zeta(x,z;L_{CP})|_{pLSM} = 1, \\ 4 & \text{where } \zeta(x,z;L_{CP})|_{pVLSM} = 1. \end{cases} \tag{3.6}$$

The velocity perturbations associated with each motion can thus be conditionally sampled based on the area indicator I. For example, the streamwise velocity fluctuation u corresponding to the specific motion (I) is expressed as $u_I(x, z; y_{ref}) = u(x, y_{ref}, z) \mid I(x, z)$, where y_{ref} is 0.15δ. The conditional sampling was performed using the instantaneous raw streamwise velocity fluctuations u, and the results were differentiated into the four categories given by (3.6).

3.2. *Conditional velocity correlations*

The spatial characteristics of long-u streaks are explored by computing the conditional two-point correlations. For the streamwise structures (u_I) identified by the area indicator function I, the conditional correlation coefficient (R) with the fluctuating velocity field (u_j) is defined as

$$R[u_I, u_j](r_x, y, r_z; y_{ref}) = \frac{\langle u_I(x, z; y_{ref}) u_j(x + r_x, y, z + r_z) \rangle}{\sigma_{u_I}(y_{ref}) \sigma_j(y)}, \tag{3.7}$$

where the subscript j represents different components of the velocity perturbations (u, v, w) and σ is the standard deviation. For brevity, we will refer to R simply as the correlation. The present conditional correlations (3.7) are similar to the expression by Ganapathisubramani (2008), who studied the velocity field in the vicinity of momentum sources and sinks. The evaluation of $R[u_I, u_j]$ reflects the fluctuating velocity field associated with the specific events (u_I), which can reveal the statistical structure of the flow around the long-u motions.

Figure 4 shows the 3D representation of the conditional two-point correlations $R[u_I, u]$ at $y_{ref}/\delta = 0.15$ with the contour lines in the x–y plane ($r_z/\delta = 0$). There is a positive isosurface of the correlations elongated in the streamwise direction and inclined with respect to the wall. The positive values have a ramp-like shape, which is a general feature of the unconditional two-point correlations ($R[u, u]$) in the log layer (Hutchins & Marusic 2007*a*; Lee & Sung 2011; Baltzer *et al.* 2013). Despite the general similarities to the characteristics of the unconditional correlation ($R[u, u]$), the magnitude and shape of $R[u_I, u]$ depend on the conditions. In particular, the correlations of nVLSM ($R[u_2, u]$) and pLSM ($R[u_3, u]$) have higher values and longer isosurfaces than the others, indicating that those structures are the most strongly correlated with the surrounding perturbation fields. The correlation of nVLSMs

https://doi.org/10.1017/jfm.2016.3 Published online by Cambridge University Press

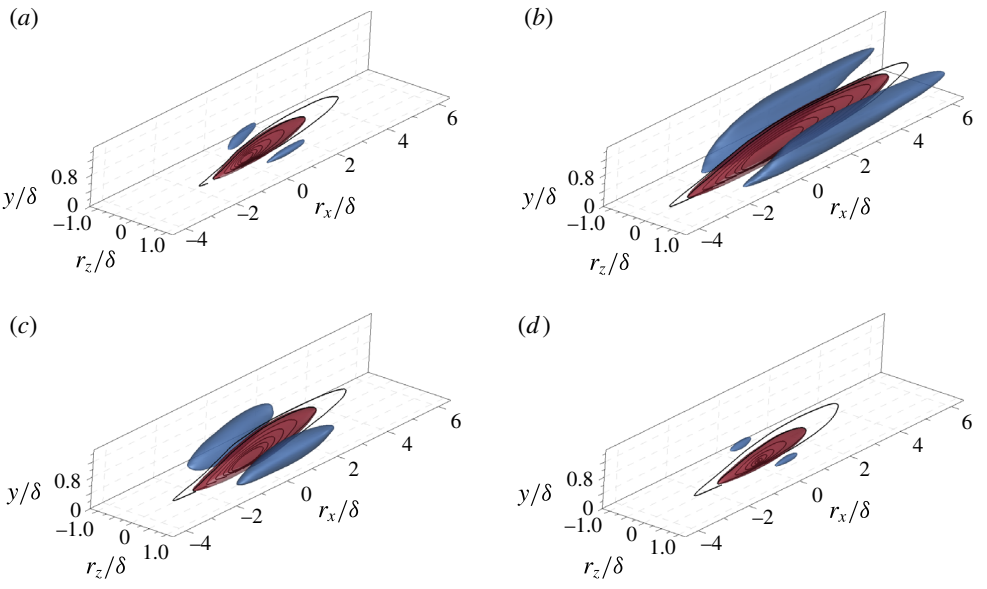


FIGURE 4. (Colour online) Conditional correlations of the streamwise velocity fluctuations, $R[u_I, u]$, in 3D perspective view: (*a*) nLSM (u_1); (*b*) nVLSM (u_2); (*c*) pLSM (u_3); and (*d*) pVLSM (u_4). The isosurfaces mark $R[u_I, u] = 0.03$ (red) and -0.015 (blue). The inserted contour lines represent $R[u_I, u]$ in the x–y plane ($r_z/\delta = 0$) and range from 0.02 to 0.08 with an increment of 0.01.

extends longer than that of nLSMs in the upstream and downstream directions (10δ and 6δ for each case based on $R = 0.02$), and the maximum correlation values for nLSM and nVLSM are 0.12 and 0.17, respectively. The streamwise velocity fluctuations are more correlated with nVLSMs in both the streamwise and wall-normal directions, although the population of nVLSMs is less dominant than that of nLSMs in the log region as shown in figure 2(*a*). In addition, the correlation of nLSMs is inclined at a larger angle ($\sim 8°$) in the streamwise direction compared to the nVLSMs ($\sim 6°$). The ramp-like character of the correlations indicates that nLSMs and nVLSMs are correlated with the streamwise fluctuations in both the near-wall and core regions along the streamwise direction. The correlations are extended as footprints down to the wall and the footprint of nVLSMs is more evident than that of nLSMs. The conditional correlations of the positive-u conditions (pLSM and pVLSM) are illustrated in figure 4(*c*,*d*). The correlations of pLSMs are more dominant than those of pVLSMs; the maximum correlation values are 0.16 and 0.09 and persist over streamwise extents of 7δ and 5δ, respectively. The pLSMs are organized motions of the positive-u regions in the log layer, and this result is also consistent with the population trend and the dominant area fraction of pLSMs (14.5 %) relative to pVLSMs (5 %) at $y/\delta = 0.15$ (figure 2*a*,*c*).

Figure 5(*a*,*b*) displays the spatial organization of the correlations in the cross-flow plane ($r_x/\delta = 0$). Note that the correlations are shown side by side in each panel, with LSMs on the left (red) and VLSMs on the right (blue) since each is symmetric in the spanwise direction. The heights of the positive correlations ($r_z/\delta = 0$) are 0.55δ (nLSM) and 0.8δ (nVLSM), indicating the dominance of nVLSMs up to the core region of the channel flow. The positive correlations with width $\Delta z/\delta \approx 0.3$ are centred

https://doi.org/10.1017/jfm.2016.3 Published online by Cambridge University Press

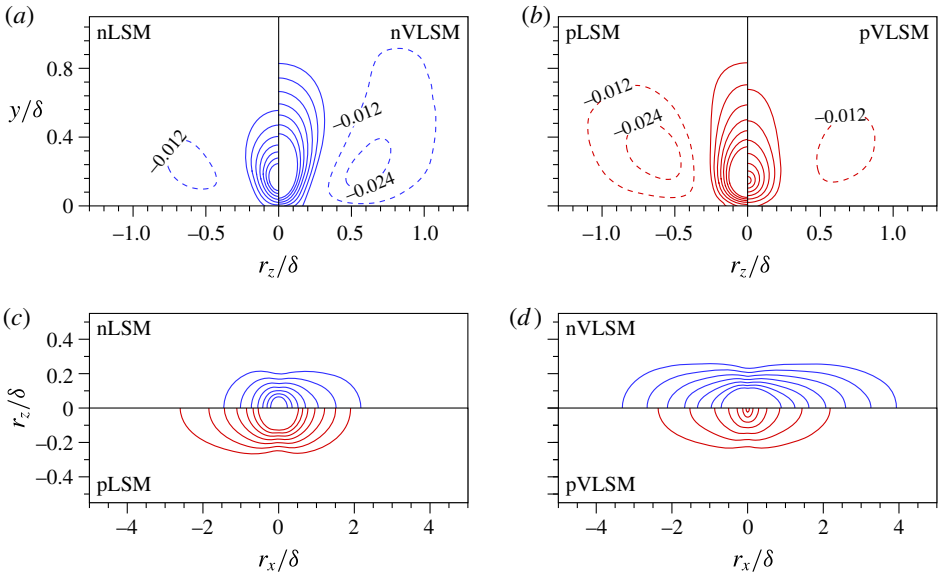


FIGURE 5. (Colour online) Conditional correlations $R[u_I, u]$, (*a*,*b*) in the y–z plane ($r_x/\delta = 0$) and (*c*,*d*) in the x–z plane ($y = y_{ref}$): (*a*) nLSM (u_1) and nVLSM (u_2); (*b*) pLSM (u_3) and pVLSM (u_4); (*c*) nLSM (u_1) and pLSM (u_3); and (*d*) nVLSM (u_2) and pVLSM (u_4). The blue and red lines represent the negative- and positive-u conditions. The positive contours (solid) range from 0.02 to 0.08 with an increment of 0.01 and the values of the negative contours (dashed) are reported in (*a*,*b*).

at the reference position and are flanked on both sides by weaker negative values at a distance of the order of 1δ. The anticorrelated regions of nVLSMs are similar in height compared to the positive correlation. The distinct negative patterns observed in the correlations of nVLSMs show that relatively strong positive-u structures are flanked on both sides of nVLSMs. A comparable spanwise size of the conditional correlations of the nLSMs and nVLSMs ($\Delta z/\delta \sim 0.3$) indicates that the two classes of structures have similar spanwise scales, which is a prerequisite for VLSMs to be formed by the streamwise concatenation of LSMs (Kim & Adrian 1999).

The conditional correlations of pLSMs and pVLSMs are illustrated in figure 5(*b*). The correlation of pLSMs reaches up to the core region similar to nVLSMs. However, the patterns of the positive-u correlations (figure 5*b*) differ appreciably in the wall-normal direction from the negative-u correlations (figure 5*a*). They retain their width along the wall-normal direction while their negative counterparts gradually decrease close to the wall. In other words, the footprint of the positive-u structure is wider than that of the negative-u one, which suggests that the near-wall region which is affected by the outer large scales is larger for positive-u motions; this point will be discussed in detail in § 3.3.

Wall-parallel cross-sections ($y = y_{ref}$) of the correlations are presented in figure 5(*c*,*d*). The correlations of LSMs (figure 5*c*) show a bias: the pLSM is biased in the upstream direction whereas the nLSM is biased downstream. However, the correlations of VLSMs are nearly symmetric in the streamwise direction (figure 5*d*). Lee & Sung (2013) also reported a bias in the correlation when conditioned on the sign of u only (but not the size of the structure). The present results thus attribute this bias to the dominant contribution by u regions with length 1–3δ (LSMs). In addition, the

https://doi.org/10.1017/jfm.2016.3 Published online by Cambridge University Press

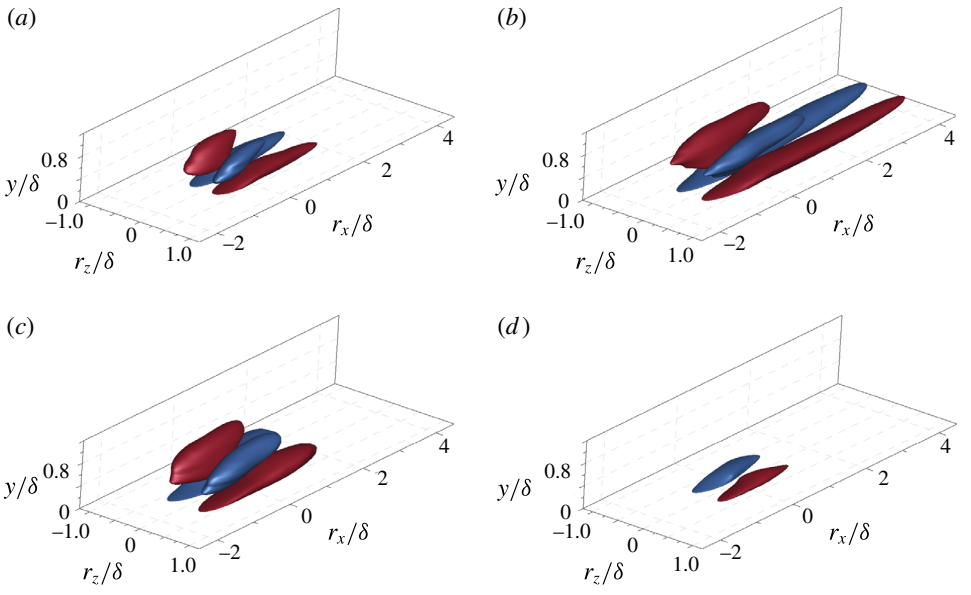


FIGURE 6. (Colour online) Conditional cross-correlations, $R[u_I, w]$, in 3D perspective view: (*a*) nLSM (u_1); (*b*) nVLSM (u_2); (*c*) pLSM (u_3); and (*d*) pVLSM (u_4). The red and blue isosurfaces are $R[u_I, w] = 0.01$ and -0.01, respectively.

correlations that represent the prominent length scales in the streamwise and spanwise directions are pLSMs and nVLSMs (figure 5*c*,*d*). Lee & Sung (2013) and Sillero *et al.* (2014) used the two-point correlation to estimate the streamwise and spanwise length scales at various wall-normal locations. They found that the negative-u structures are slightly longer and narrower than the positive-u ones. The present correlations reveal that the relatively longer (negative-u) and wider (positive-u) length scales observed in those previous studies are due to the contributions of nVLSMs and pLSMs, respectively.

Next, the conditional cross-correlations between the specific u events and the spanwise velocity fluctuations (w), $R[u_I, w]$, are examined. The 3D representations of $R[u_I, w]$ are illustrated in figure 6. Each of figures 6(*a*)–6(*c*) includes four isosurfaces, two of which are attached to the wall. Figure 6(*d*) for pVLSM only displays two isosurfaces due to the weak correlation level. The sign of the correlation reflects the dominant direction of spanwise velocity fluctuations associated with the u events. For the negative-u events, the positive correlation is associated with negative w and the anticorrelation corresponds to positive w. In other words, the attached and detached pairs represent converging and diverging motions in the spanwise direction, respectively. The interpretation of the sign of the correlation reverses for positive-u events. A clear feature of these correlations is their elevated levels below the reference position, close to the wall. The streamwisely organized motions in the log layer have a strong correlation with the near-wall spanwise velocity fluctuations. The $R[u_2, w]$ (nVLSM), in particular, shows a very long streamwise extent of attached isosurfaces. For positive u, $R[u_3, w]$ (pLSM) shows highly correlated regions relative to $R[u_4, w]$ (pVLSM) and the attached pairs are more elongated upstream than downstream.

To investigate the cross-correlation $R[u_I, w]$ in further detail, a cross-section at $r_x/\delta = 0$ is shown in figure 7. As illustrated by the filled contours, the attached pairs

https://doi.org/10.1017/jfm.2016.3 Published online by Cambridge University Press

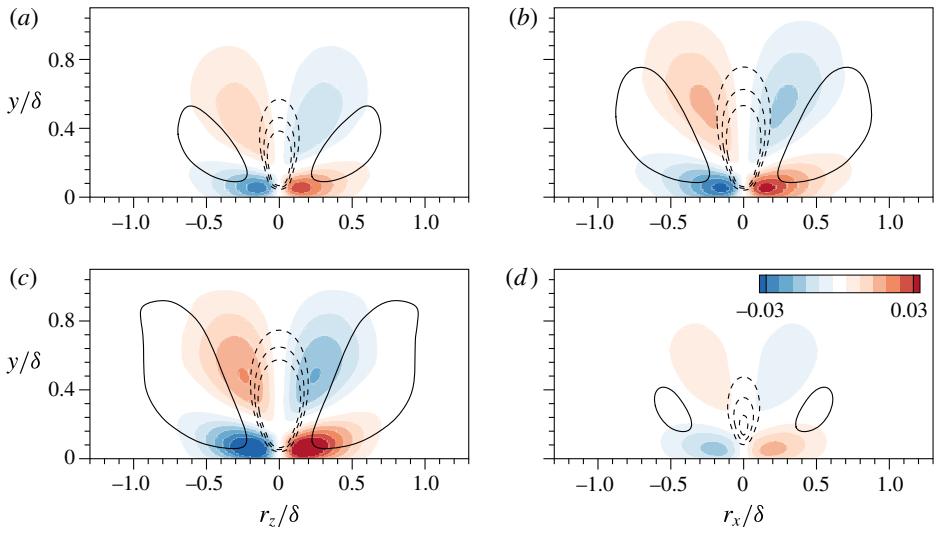


FIGURE 7. (Colour online) Conditional correlations ($R[u_I, w]$) in the y–z plane ($r_x/\delta = 0$): (*a*) nLSM (u_1); (*b*) nVLSM (u_2); (*c*) pLSM (u_3); and (*d*) pVLSM (u_4). The filled contours are $R[u_I, w] = \pm(0.005 : 0.005 : 0.03)$. The inserted line contours represent $R[u_I, v]$ varied from -0.015 to -0.025 with an interval of 0.005 (dashed) and $R[u_I, v] = 0.006$ (solid).

have larger correlations close to the wall and their peaks occur at $y^+ = 42$ even though the reference position of the events is located at $y/\delta = 0.15$. Compared to the negative values of $R[u_I, v]$ (dashed lines), the spanwise velocity fluctuations penetrate more deeply towards the wall, which reflects that the footprints of outer large-scale structures are more directly related to near-wall spanwise velocity fluctuations – a result that is consistent with the amplitude modulation of w recently reported by Talluru *et al.* (2014). The spanwise locations of the peaks are $r_z/\delta = \pm 0.13$ and ± 0.18 for the negative- and positive-u events, respectively. In other words, the peak distance is wider for the positive-u events due to the dispersive motions in the spanwise direction, indicating that the outer large-scale positive u could affect near-wall w over a larger spanwise extent. Additionally, the contours of $R[u_I, u]$ for negative u are gradually narrower under the reference position whereas those for positive u are relatively wider in figure 5(*a*,*b*). This difference in the shape is due to the opposite direction of spanwise motions in the vicinity of the wall; the congregative motions for negative-u and dispersive for positive-u footprints.

The line contours of $R[u_I, v]$ which represent the wall-normal fluctuations (v) associated with specific u events are displayed in figure 7. Around the reference point, the correlations are negative, which is characteristic of Q2 ejections ($u < 0$ and $v > 0$) for the outward motions and Q4 sweeps ($u > 0$ and $v < 0$) for the inward motions (Wallace, Eckelmann & Brodkey 1972). In particular, nVLSMs and pLSMs are most strongly correlated to the surrounding wall-normal fluctuations, $R[u_2, v]$ and $R[u_3, v]$. The Reynolds shear stress associated with the ejection and sweep events is therefore dominated by nVLSMs and pLSMs in the log layer. By comparing $R[u_I, v]$ with $R[u_I, w]$, a pair of large-scale circulations is observed on both sides of the ejection (negative-u condition) and sweep (positive-u condition). The association between low-speed, large-scale structures and a pair of counter-rotating roll modes was reported in previous studies (e.g. Hutchins & Marusic 2007*b*;

https://doi.org/10.1017/jfm.2016.3 Published online by Cambridge University Press

Chung & McKeon 2010; Baltzer *et al.* 2013; Talluru *et al.* 2014). Those works mentioned that large-scale circulations have an important influence on the near-wall fluctuations. These opposite wall-normal motions of ejections ($v > 0$) and sweeps ($v < 0$) each induce opposite spanwise near-wall movements, which can be described as congregative and dispersive, respectively. This highlights an important difference in inner–outer interactions involving large-scale low- versus high-speed events. In addition, the maximum correlation values for nLSM ($R[u_1, w]$) and nVLSM ($R[u_2, w]$) are 0.034 and 0.048, respectively, which suggests that the strong congregative motions reside under the nVLSM. In common with $R[u_l, u]$, the pLSM has the greater maximum value (0.05) relative to the pVLSM (0.025). Hence, the nVLSM and pLSM are the dominant structures that have an effect on the near-wall spanwise velocity fluctuations by inducing strong converging and diverging motions in the near-wall region. In the next section, the influence of the footprints of nVLSM and pLSM are examined by conditionally sampling the near-wall fluctuations that are associated with outer large-scale structures.

3.3. *Footprint of outer large-scale structures*

The large-scale features with streamwise extent over 1δ are frequently observed near the top of the log layer. Very long motions ($>3\delta$), in particular, are predominantly low-speed events compared to high-speed ones (figure 2). Figure 8(*a*) shows the streamwise velocity fluctuations in the wall-parallel plane $y/\delta = 0.15$. There are several elongated structures of negative and positive u with stripiness over the plane and long low-speed structures are flanked by relatively short high-speed regions. The inserted line represents a conditionally sampled low-speed event with length over 21δ. This structure is visibly similar (typically $O(20\delta)$ in length) to that reported by Monty *et al.* (2007) and by Hutchins & Marusic (2007*a*), although the present structure is identified using a different technique. Hutchins & Marusic (2007*a*) applied a Gaussian filter in two planes, located in the log and buffer regions of turbulent channel data, and noted the visual similarity between the velocity patterns for both wall-normal positions. They interpreted their observation as the footprints of very long low-speed regions extending down to very near the wall. In figure 8(*b*) the streamwise velocity fluctuations are plotted at $y^+ = 14.5$. To identify the near-wall regions associated with outer large-scale events (footprints), we conditionally sampled the near-wall *CP* lines (shown in figure 8*c*), which are vertically connected to the long *CP* lines ($L_{CP} > 1\delta$) at $y/\delta = 0.15$. The procedure of the footprint identification is summarized below.

(1) As noted in § 2.2, the contiguous regions of streamwise velocity fluctuations are identified based on the *CP* in the wall-parallel plane at $y/\delta = 0.15$. By measuring the streamwise length of the signed *CP* (L_{CP}), the u streaks are conditionally sampled in the flow field.

(2) To identify the near-wall extent of these long u motions, the connectivity of the *CP*s is traced in the wall-normal direction by comparing adjacent wall-parallel planes (j and $j-1$ planes). Neighbouring *CP*s connected in the $j-1$ plane are continuously identified down to the wall.

(3) Among the near-wall *CP*s (figure 8*c*), only those that are vertically connected to the reference *CP* are conditionally sampled (black lines in figure 8*d*). The areas of the near-wall *CP*s are determined by measuring their lower and upper bounds similar to figure 1(*c*). In this manner, we quantify the footprints of outer long u motions, as marked by the grey shading in figure 8(*d*).

https://doi.org/10.1017/jfm.2016.3 Published online by Cambridge University Press

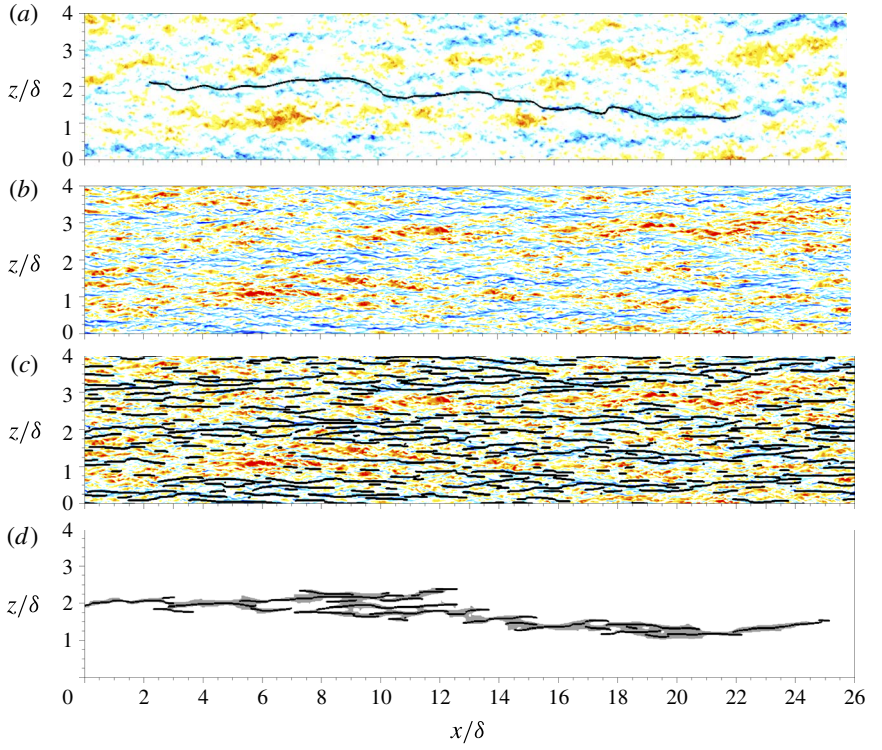


FIGURE 8. (Colour online) Instantaneous flow fields in the x–z plane. The contours show the streamwise velocity fluctuations at (*a*) $y/\delta = 0.15$ and (*b–d*) $y^+ = 14.5$. In (*a*), the inserted solid line ($CP = -1$) identifies an nVLSM with 21δ. The lines in (*c*) mark $CP = -1$ in that wall-parallel plane. In (*d*), at $y^+ = 14.5$, the solid lines identify the near-wall *CP* that are vertically connected to the line that marks the nVLSM in (*a*).

The detected footprint of nVLSMs (grey area in figure 8*d*) is remarkably similar to its outer low-speed event. The collective length of the near-wall *CP*s is over 20δ. This near-wall arrangement affirms the correlation between near-wall and outer structures, and the view that the near-wall ones are modulated by the outer large scales, consistent with Hutchins & Marusic (2007*b*) and Mathis *et al.* (2009). To examine this relation further, the near-wall regions which are connected to outer large-scale structures are conditionally sampled from each instantaneous field and their characteristics are analysed.

Figure 9 shows the joint probability density function (joint p.d.f.) of (*a*) u–v and (*b*) u–w at $y^+ = 14.5$. The velocity fluctuations associated with the footprints are identified using the conditionally sampled *CP*s in the near-wall region. Here, the joint p.d.f.s of the nVLSMs (blue) and pLSMs (red) are shown because these are the dominant motions that have an influence on the near-wall region (cf. § 3.2). The joint p.d.f. of u–v is presented in figure 9(*a*) and the adjacent upper (right) panel shows the p.d.f. of u (v). Ejections and sweeps are the principal perturbations on the footprints of nVLSM and pLSM, respectively. However, their distributions are not symmetric with respect to the origin; the contour line of the pLSMs reaches $u^+ = 8$ and $v^+ = -1.8$, whereas that of the nVLSMs reaches $u^+ = 7$ and $v^+ = -1.8$. This difference also appears as a spread in the u and v p.d.f.s of the pLSMs. The inserted

https://doi.org/10.1017/jfm.2016.3 Published online by Cambridge University Press

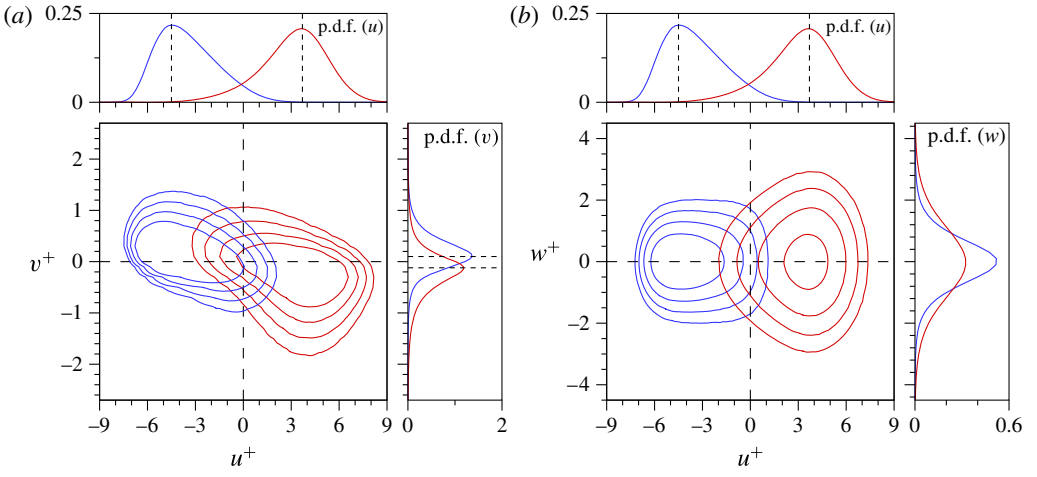


FIGURE 9. (Colour online) Joint p.d.f.s of (*a*) u–v and (*b*) u–w at $y^+ = 14.5$. The thinner upper panels show the p.d.f. of u and the thinner right panels show the p.d.f. of v and w. The velocity fluctuations are computed from the detected near-wall *CP*s, which are vertically connected to the outer structures. The blue and red lines represent the velocity fluctuations associated with the footprints of nVLSM (blue) and pLSM (red), respectively. Contour levels are distributed exponentially from 0.005 to 0.05.

lines mark the peak locations of the p.d.f.s; the characteristic u of the footprint of nVLSMs ($u^+ = -4.5$) is greater than that of the pLSMs ($u^+ = 3.7$). The asymmetry between negative- and positive-u events demonstrates that the influence of large-scale structures depends on their sign, consistent with the work by Agostini & Leschziner (2014). This trend is prominent in the joint p.d.f. of u–w (figure 9*b*). The w of pLSMs are widely distributed, while those of nVLSMs are narrowly distributed. The intense w are apparent on the footprints of the large-scale positive-u event. The wider (narrower) distributions for the pLSMs (nVLSMs) arise due to the spanwise dispersive (congregative) motions shown in figure 7.

In order to quantify the contributions of the various outer events to the Reynolds shear stress, the weighted joint p.d.f. of u–v is shown in figure 10(*a*). The weighted joint p.d.f. is computed by multiplying the joint p.d.f. by uv. Note that the results for nVLSM and pLSM are plotted side by side in each panel, with nVLSMs at left and pLSMs at right. The maximum values of the weighted joint p.d.f. are denoted by the black filled circles. For the nVLSMs, the maximum values are $u^+ = -4.75$ and $v^+ = -0.35$, which are located in the second quadrant. In contrast, the maximum is $v^+ = -0.5$ for the pLSMs. These strong downward motions driven by sweeps of outer positive u lead to intense velocity fluctuations even inside the viscous sublayer (not shown here). The difference between the nVLSMs and pLSMs is also apparent in the spanwise velocity fluctuations. Figure 10(*b*) shows the weighted joint p.d.f. of u–w, where w on the footprints of the pLSMs are clearly greater than those of the nVLSMs. The maximum values of the spanwise component are ± 1.15 and ± 0.7 for pLSMs and nVLSMs, respectively. The outer large-scale positive-u event not only strengthens the near-wall u, but also enhances the near-wall w. The w are appreciably modulated by the pLSMs, even more than u and v; this is the origin of the highest amplitude modulation coefficient for w in the near-wall region, which was reported by Talluru *et al.* (2014). In addition, the discrepancy in the distributions of outer positive- and

https://doi.org/10.1017/jfm.2016.3 Published online by Cambridge University Press

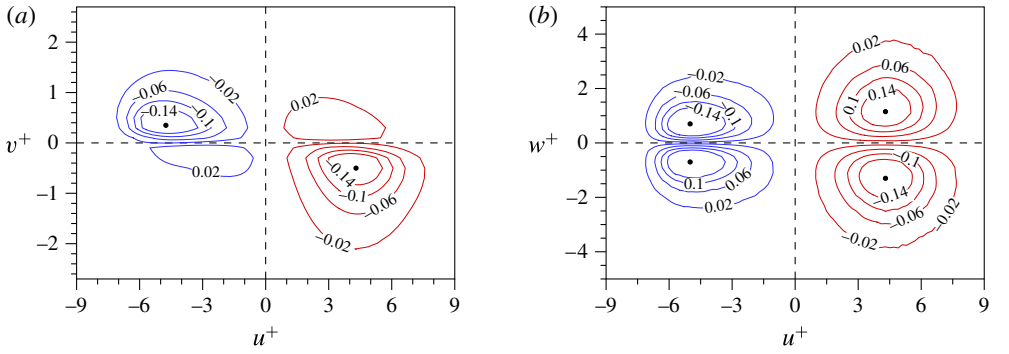


FIGURE 10. (Colour online) Weighted joint p.d.f.s of (*a*) u–v and (*b*) u–w at $y^+ = 14.5$. The velocity fluctuations are computed from the detected near-wall *CP*s, which are vertically connected to the outer structures. The blue and red lines represent the velocity fluctuations associated with the footprints of nVLSM (blue) and pLSM (red), respectively. The black circles mark the maximum value of the velocity fluctuations.

negative-u events in figure 10(*b*) reflects that the downward motions carried by the positive-u structures (sweeps) move the higher-momentum fluid towards the wall where it is spread laterally.

To examine the flow field around the footprints of nVLSM ($u_I = 2$) and pLSM ($u_I = 3$), the conditionally averaged velocity is defined,

$$\boldsymbol{u}|_{FP_I}(r_x, y, r_z) = \langle \boldsymbol{u}(x + r_x, y, z + r_z)|CP_I(x, y_{ref}, z)\rangle, \tag{3.8}$$

where CP_I denotes the streaks that are vertically connected to the outer large scales (u_I). The reference wall-normal position is $y^+_{ref} = 14.5$. Figure 11(*a*,*c*) illustrates isosurfaces of conditional streamwise velocity fluctuation $u|_{FP_I}$. Although the reference wall-normal position was chosen at $y^+_{ref} = 14.5$, the conditional structures have long streamwise lengths, extending over 4δ (nVLSM) and 2δ (pLSM) in the streamwise direction. On the contrary, the conditional averages based on the negative- and positive-u streaks that are not connected to the outer large-scale events ($u|_{NWS}$) have streamwise lengths of approximately 1000 wall units and are confined within the near-wall region. Figure 11 clearly shows the scale separation in the near-wall region. In addition, the black isosurface represents the swirling strength educed of the conditionally averaged fields (Zhou *et al.* 1999). Conditional structures of both nVLSMs and pLSMs have a long pair of roll modes on both sides of large negative- and positive-u structures. These large-scale circulations are quite different from the smaller rolls associated with the velocity contours of $\boldsymbol{u}|_{NWS}$ and which are shown in the zoomed view (insets of figure 11*b*,*d*). The centres of the small rolls are located at $y^+ = 40$ and $r^+_z = 50$ while those of large-scale circulations are located at $y/\delta = 0.2$ and their spanwise width is 0.4δ. Although the large-scale circulations of negative- and positive-u structures have similar widths, the maximum swirling strength of the pLSM is 1.3 times greater than that of the nVLSM.

3.4. *Formation of long negative-u structure*

The previous section demonstrated that long negative-u structures ($>3\delta$) are frequently observed in the log layer compared to positive-u ones which prevail in relatively short

https://doi.org/10.1017/jfm.2016.3 Published online by Cambridge University Press

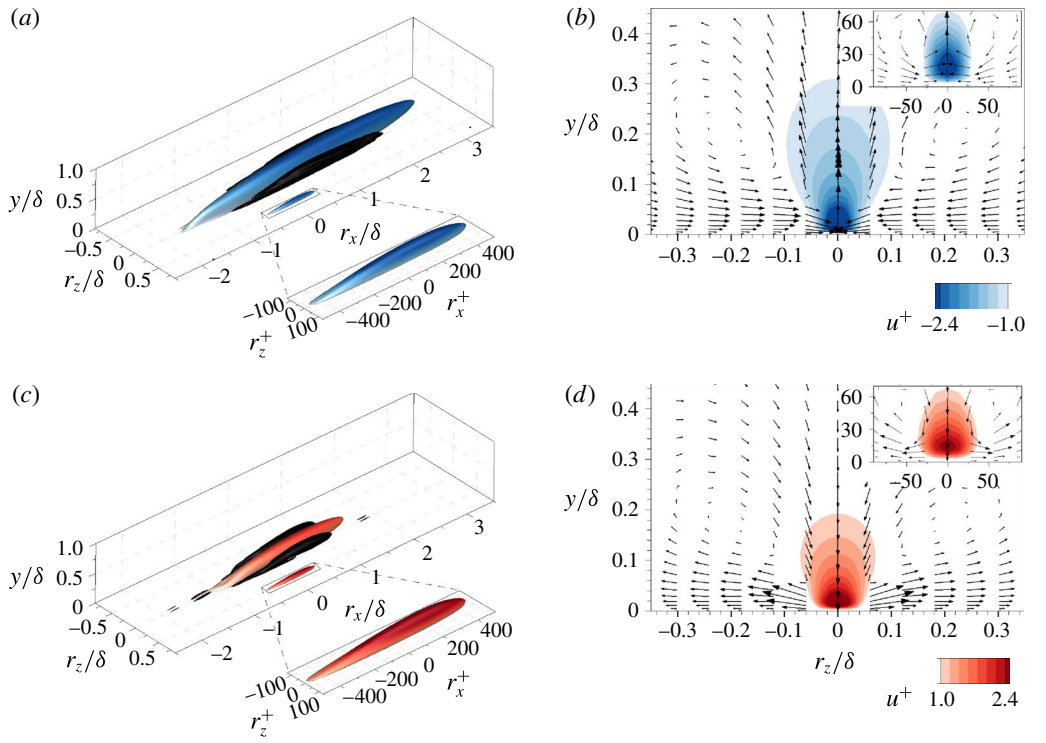


FIGURE 11. (Colour online) Conditional structures associated with the footprints of nVLSMs (*a*,*b*) and pLSMs (*c*,*d*) at $y^+ = 14.5$. (*a*,*c*) Isosurfaces of the streamwise velocity fluctuations $u^+|_{FP_I} = -1.0$ (blue) and $+1.0$ (red). Black isosurfaces are 7 % of the maximum swirling strength. The conditional structures of near-wall streaks that are not connected to outer large scales ($u^+|_{NWS}$) are shifted in the spanwise direction by 0.5δ and their magnified views are shown in wall units. (*b*,*d*) Conditionally averaged fields in the y–z plane ($r_x/\delta = 0$). Vectors represent the in-plane velocity components.

streamwise extent ($<3\delta$). The analysis also showed that the different flow patterns around u_I contribute to their distinct near-wall signatures, i.e. congregative versus dispersive. This section focuses on the long negative-u structures ($>3\delta$) linked with a pair of large-scale circulations around those structures in order to explain their dominance compared to the positive counterparts. The work by Lee *et al.* (2014) provides an important background. They found that the low-speed regions with lengths 1–3δ dominantly undergo merging, and that the merging process was facilitated by the different convection velocities between the upstream and downstream structures. Using conditional spatiotemporal correlations of negative-u structures, they showed that the convection velocities of the structures depend on their strength, u: weak negative-u structures have a relatively higher convection velocity than strong negative-u ones. To understand the merging process, it is necessary to explain the cause of the variation in the strength of u between the tail and the head of the two structures involved.

The merging process of two low-speed structures is captured in figure 12. The blue isosurface represents the outer region, $y/\delta \geqslant 0.1$. Initially a gap with streamwise length of the order of 0.5δ separates the upstream and downstream structures (figure 12*a*). At $t = t_{ref}$, the outer structures start to merge by narrowing the gap, and ultimately form a very long negative-u structure. During the merging process, the tail of the downstream

https://doi.org/10.1017/jfm.2016.3 Published online by Cambridge University Press

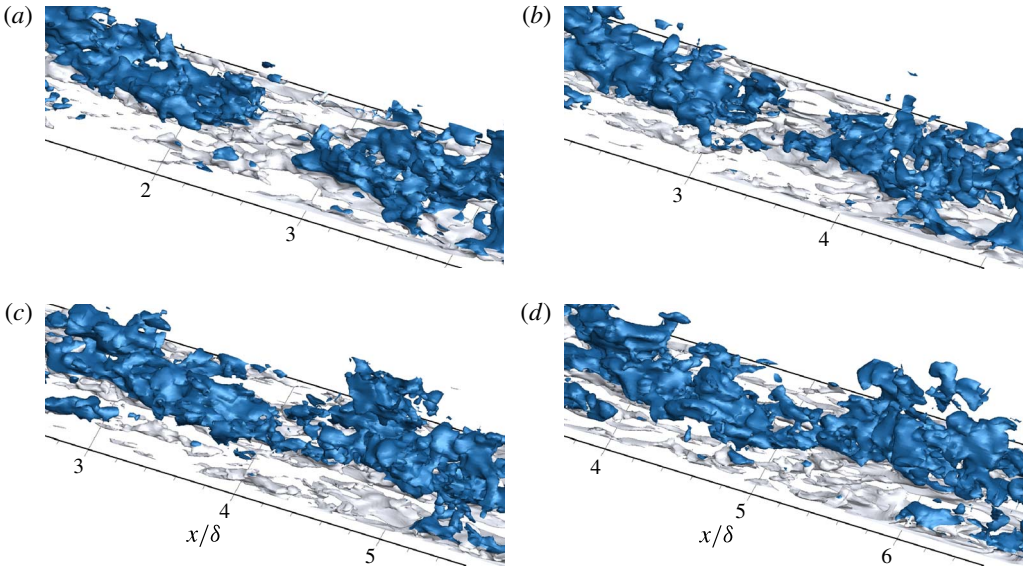


FIGURE 12. (Colour online) Three-dimensional isosurfaces of negative-u structures ($u = -0.9u_{th,raw}$). The time of each instantaneous field is: (*a*) $t_{ref} - 3.0\delta/U_{CL}$, (*b*) $t_{ref} - 1.5\delta/U_{CL}$, (*c*) t_{ref} and (*d*) $t_{ref} + 1.5\delta/U_{CL}$. The isosurfaces are coloured according to their wall-normal distance: $y/\delta < 0.1$ (white) and $y/\delta \geqslant 0.1$ (blue).

structure has a slower convective speed than the head of the upstream one. The slower convection speed of the downstream structure is partly due to the relatively higher magnitude of u in that region relative to around the head of the upstream structure. However, the origin of this difference in u is unclear and, in light of the correlation between the events in the outer and near-wall flow, a simultaneous investigation of the two regions during the merging process is required. We will demonstrate that this merging process is tightly connected to the spanwise congregative motion under the footprint of large-scale low-speed event.

3.4.1. *Time-evolving fields*

A time series of the velocity perturbation field is shown in figure 13, and captures the merging of two LSMs at $y/\delta = 0.15$. The black lines in figure 13(*a*) mark the *CP* in the wall-parallel plane, and represent continuous regions of negative u. At $t_{ref} - 1.5\delta/U_{CL}$, there are two distinct LSMs, which are marked 'A' and 'B', and which are not connected to each other; they are separated by a region of positive velocity perturbation. The streamwise lengths of the upstream LSM-A and the downstream LSM-B are of the order of 1–2δ, and their spanwise widths are approximately 0.4δ. They advect in the downstream direction with different speeds, with 'A' moving faster than 'B' even when visualized in the same wall-parallel plane. The downstream structure (LSM-B) is continuously stretched due to the slower advection velocity of its tail relative to its head. On the other hand, LSM-A maintains its length. The gap between the two structures progressively narrows, and they ultimately merge into a single long streak whose streamwise extent is longer than 3δ. The evolution of the near-wall perturbation field during the outer merging process is illustrated in figure 13(*b*). The black dot identifies the tail position of the LSM-B, and the vertical

https://doi.org/10.1017/jfm.2016.3 Published online by Cambridge University Press

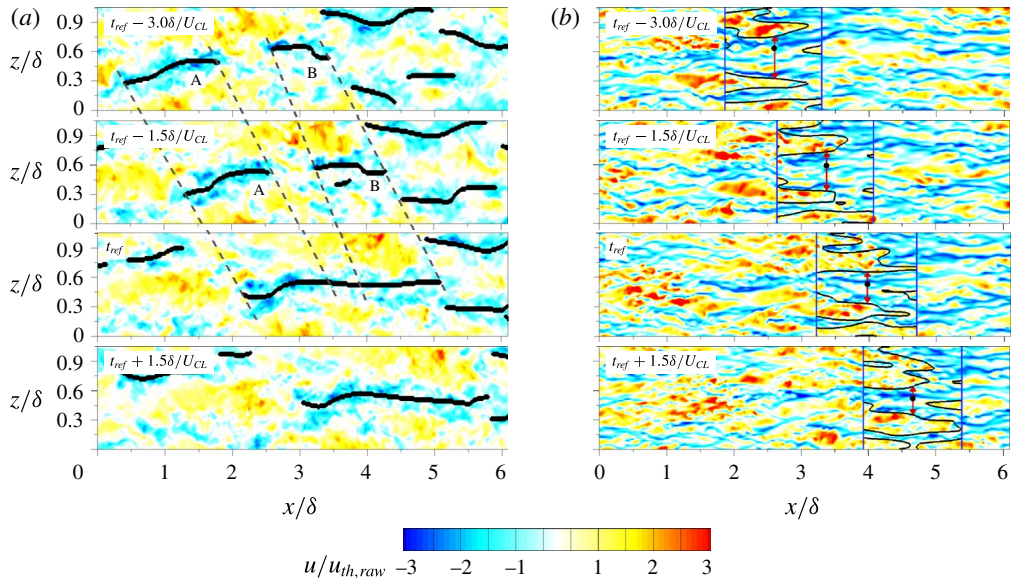


FIGURE 13. (Colour online) Time sequence of instantaneous flow fields in the x–z plane: (*a*) $y/\delta = 0.15$ and (*b*) $y^+ = 14.5$. The time of each instantaneous field is marked in each panel. The labels 'A' and 'B' identify the upstream and downstream LSMs, respectively. In (*a*), the dashed lines are added to indicate the head and tail positions of the LSMs. In (*b*), the black circles are the tail positions of LSM-B and the black solid lines indicate $\hat{u} = 0$.

blue lines are inserted to isolate a region of length 1.5δ beneath the LSM-B. The solid black isocontour marks $\hat{u} = 0$. In the marked region, several streaky structures of negative u are distributed in the span, separated by a weak perturbation field, and each is initially narrow in width. As the outer LSMs approach one another in the merging process, the near-wall structures congregate within a narrowing window (shown by the blue arrows) and will ultimately form a wide high-amplitude negative-u region in the vicinity of the black dot.

To observe this process in detail, the time sequence of relatively strong near-wall perturbations is shown in figure 14(*a*). Here, the blue contours illustrate the near-wall streamwise velocity fluctuations lower than $-0.2U_b$, which is 1.5 times larger than the local streamwise turbulence intensity. The solid lines are inserted to highlight the behaviour of near-wall structures under the downstream LSM-B; the streamwise distance between the lines is 1000 wall units. Within the bounds of the vertical solid lines, several strong streaky structures are distributed around the dark circle (the tail position of LSM-B in figure 13*a*). They gradually congregate under the tail of downstream LSM-B and then form a long streaky structure at later time; the emergent structure is highlighted by the line contour at $t = t_{ref}$ (see the supplementary movies available at http://dx.doi.org/10.1017/jfm.2016.3). The formation of concentrated low-speed regions beneath the tail of LSM-B could bring about the retardation of the trailing edge by ejecting the lower streamwise velocity fluid (Toh & Itano 2005).

Next, a cross-stream view of the tail of the LSM B is illustrated in figure 14(*b*). The streamwise position is at the tail of B, which is marked by vertical dashed lines in figure 14(*a*), and the black line displays a transverse cut of the *CP* which is vertically

https://doi.org/10.1017/jfm.2016.3 Published online by Cambridge University Press

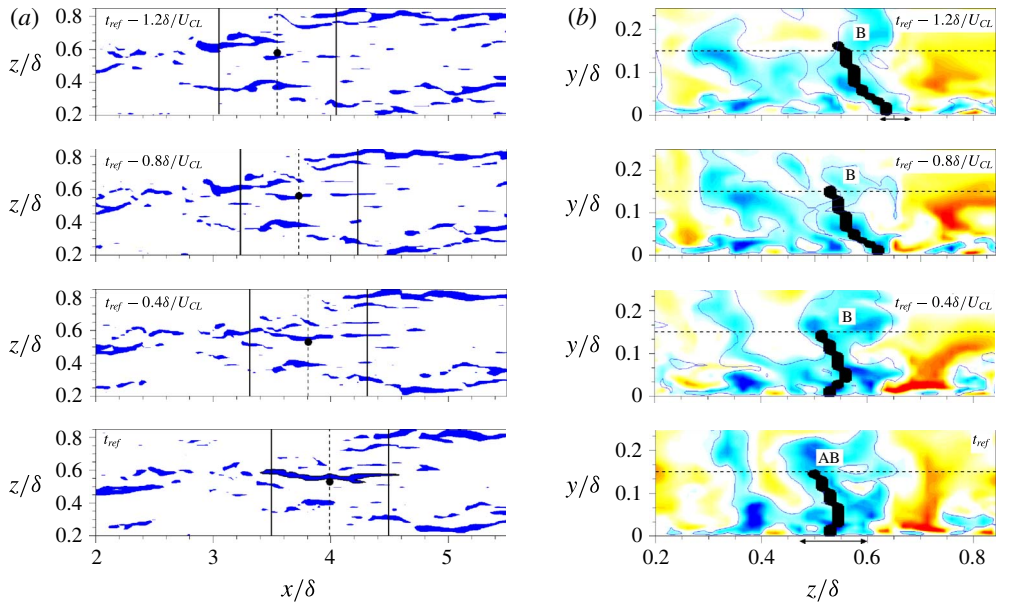


FIGURE 14. (Colour online) Time sequence of instantaneous flow fields before the merging event. (*a*) Streamwise velocity fluctuations ($u < -0.2U_b$) in the wall-parallel plane $y^+ = 14.5$. The black circles identify the tail positions of LSM-B. (*b*) Cross-stream plane at the tail position of downstream LSM-B in figure 13(*a*). The thick black lines are the cross-stream cut of the characteristic planes (*CP*). The blue line contour indicates $u = -0.05U_b$. The dashed horizontal line is at $y/\delta = 0.15$. The contour levels are consistent with figure 13. See also the supplementary movies.

connected to the outer LSM-B. The solid line extends from the wall since the LSM-B is attached to the wall. At early time, its near-wall spanwise location is $z/\delta = 0.64$ and subsequently shifts to $z/\delta = 0.53$ later in time. The height of the solid line is largely unchanged, and its terminus away from the wall is insignificantly displaced. Only its origin in the near-wall region is shifted appreciably in the span as the two LSMs A and B merge. As a result, it becomes a relatively straight line through the concentrative movement of the near-wall region under the tail of LSM-B. To highlight the variation in the spanwise size of the structure, the blue line ($u = -0.05U_b$) is inserted in the figure. At $t_{ref} - 1.2\delta/U_{CL}$, the near-wall velocity perturbation in the vicinity of the black line switches sign within $100\nu/u_\tau$ in the spanwise direction. Later in time, as the outer structures merge, the width of the near-wall negative-u region around the root of the solid line increases significantly. At $t = t_{ref}$, the width becomes 0.15δ, which is greater than the characteristic spanwise width of near-wall structures, through the spanwise merging of surrounding negative u that were initially separated by positive u.

The instantaneous realizations invoked in the above discussion suggest the possibility of a coupling between the dynamics of a large-scale structure (which induces a congregative motion) and near-wall structures during the merging of outer low-speed streaks. The near-wall negative u gradually converge under the outer low-speed region. The driving force behind this congregative motion is the outer large-scale circulations revealed in the conditional correlations in the previous section. The agglomerated negative u can lead to the much lower u around the tail of the

https://doi.org/10.1017/jfm.2016.3 Published online by Cambridge University Press

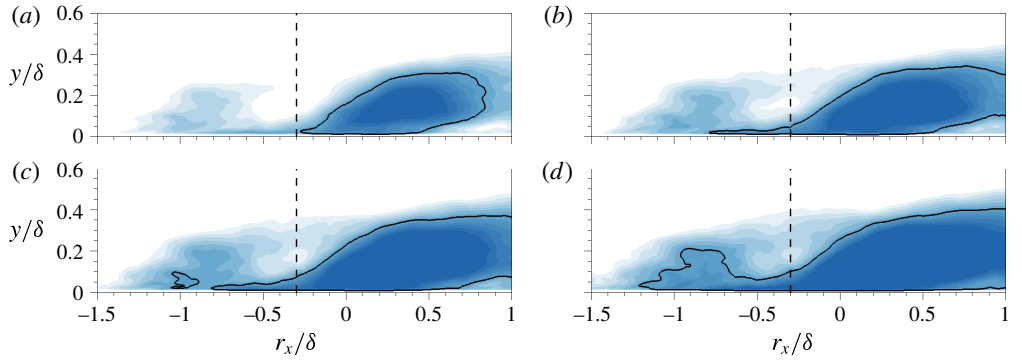


FIGURE 15. (Colour online) Time sequence of the conditionally averaged velocity fields, $u^+|_m$, in the x–y plane ($r_z/\delta = 0$): (*a*) $t_{ref} - 0.8\delta/U_{CL}$, (*b*) $t_{ref} - 0.6\delta/U_{CL}$, (*c*) $t_{ref} - 0.4\delta/U_{CL}$ and (*d*) $t_{ref} - 0.2\delta/U_{CL}$. The filled contours range from -0.76 to -1.2 with an increment of 0.04. The line isocountour is $u^+|_m = -1$.

downstream structure if ejected into the outer region. This locally different magnitude of u induces the different convection speed of the structure and causes the merging of low-speed streaks. In the remaining sections, conditionally averaged fields are examined in order to provide a statistical account of this merging process and the formation of very-long negative-u regions in the log layer.

3.4.2. *Streamwise organization of conditional structures*

The formation of very long negative-u regions ($\geqslant 3\delta$) via the merging process was conditionally sampled from the DNS time series. This enables computation of the averaged flow field associated with merging from the raw velocity fluctuations. The conditionally averaged velocity field is defined as

$$\boldsymbol{u}|_m(r_x, y, r_z; r_t) = \langle \boldsymbol{u}(x + r_x, y, z + r_z; , t - r_t) | CP^{DT}(x, y_{ref}, z; t_{ref}) \rangle, \tag{3.9}$$

where the superscript DT refers to the reference point being the tail position of the downstream structure. The reference position for the conditional averaging is $y/\delta = 0.15$ ($y^+ = 101$), and time is measured relative to a reference time, t_{ref}, where merging takes place.

A time sequence of conditionally averaged velocity fields, $u^+|_m$, is shown in figure 15. Although the reference location for the conditional average is at the tail of an outer LSM, another velocity structure of the order of 1δ in length is predicted upstream of the reference position (see figure 15*a*). At early time, the two outer structures are separated, but their relative distance decreases in time up to the merging event. The solid contour marks a relatively strong negative-u region which is initially restricted to the downstream structure but is gradually enlarged to include the upstream structure. At $t_{ref} - 0.8\delta/U_{CL}$, the most upstream position of the isocontour line represents the tail of the downstream structure, $r_x/\delta = -0.3$. As time evolves, the isocontour line extends in the upstream direction although the velocity structure convects downstream. The streamwise velocity fluctuation intensifies pronouncedly around $r_x/\delta \approx -0.3$, which is near the tail of the downstream structure: $u(r_x = -0.3, y^+ = 14.5, r_z = 0) = -1.22$ in figure 15(*d*), which is 1.3 times enhancement compared to u in figure 15(*a*). The conditionally averaged velocity fields therefore demonstrate a link between the merging of outer structures and intensifying near-wall

https://doi.org/10.1017/jfm.2016.3 Published online by Cambridge University Press

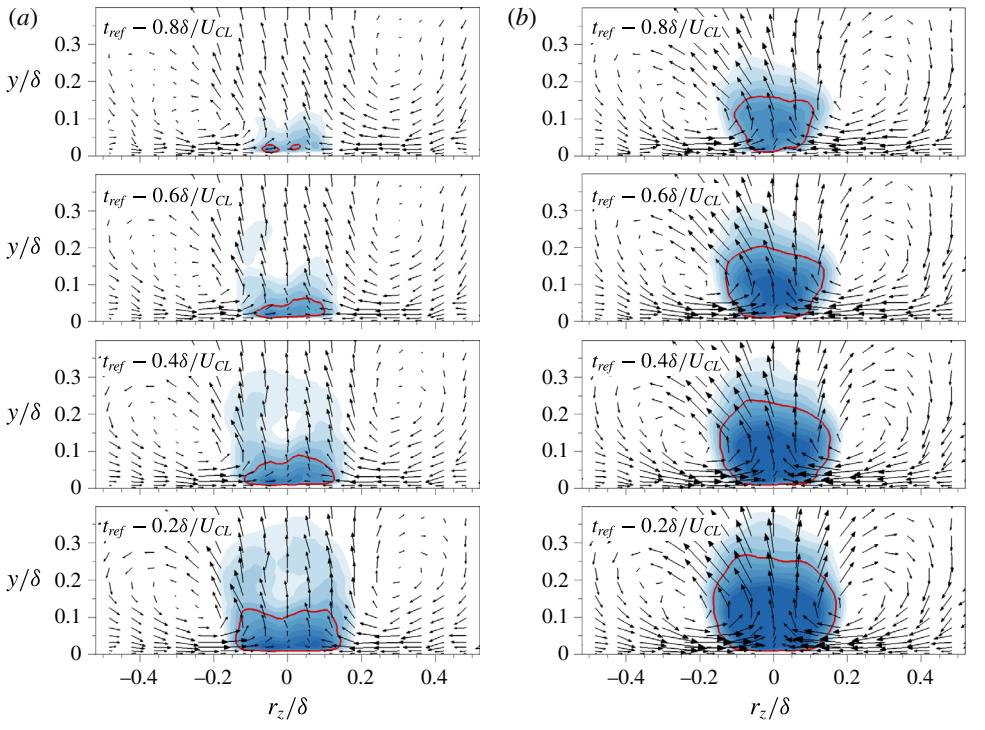


FIGURE 16. (Colour online) Time sequence of the conditionally averaged velocity fields, $u^+|_m$, in the y–z plane for (*a*) $r_x/\delta = -0.3$ and (*b*) $r_x/\delta = 0$. Filled contours range from -0.8 to -1.25 with an increment of 0.05, and vectors represent the in-plane velocity components. The red isocontour is $u^+|_m = -1$.

disturbances. In the instantaneous fields (figure 14*a*), the negative-u regions under the tail of the downstream LSM progressively intensify prior to merging. The same trends are evident in the conditionally averaged velocity, where the streamwise fluctuations in the near-wall region significantly intensify near the tail of the downstream structure and lead to a slower local convection speed.

3.4.3. *Near-wall structures and large-scale circulation*

The x–y planes of conditionally averaged fields ($u^+|_m$) demonstrated that an intense near-wall perturbation is generated at the tail of the downstream structure that partakes in the merging event. Here the focus is placed on the outer roll-cell motion, which is the driving force that leads to this strong near-wall perturbation. Figure 16 shows the time evolution of the near-wall disturbances in the y–z plane. The vectors are the conditionally averaged in-plane velocities, and the contours show the streamwise velocity perturbation. In figure 16(*a*), the reference location for conditional averaging is $r_x/\delta = -0.3$, which is marked by vertical dashed lines in figure 15. This position is the most upstream end of the strong negative disturbance ($u^+|_m = -1.0$) associated with the downstream structure at $t_{ref} - 0.8\delta U_{CL}$. The solid line shows the isocontour level $u^+|_m = -1.0$ in order to mark relatively strong streamwise perturbations, similar to figure 15. At early time, the wall-normal extent of the lowest contour level, $u^+|_m = -0.8$, is confined within $y/\delta \leqslant 0.1$. Moreover, there is a pair of large-scale circulations without a strong low-speed event – a notable feature that should be contrasted to

https://doi.org/10.1017/jfm.2016.3 Published online by Cambridge University Press

previous work on the conditional averages where rolls and low-speed structures coexist (e.g. Hutchins & Marusic 2007*b*; Chung & McKeon 2010; Baltzer *et al.* 2013; Talluru *et al.* 2014). In those studies, both the diameter and the wall-normal location of the core of the large-scale rolls increase downstream. They are therefore inclined relative to the wall at a similar angle as low-speed structures (Talluru *et al.* 2014). In contrast, the cores of the present large-scale circulations observed during the merging process are located at $y/\delta \approx 0.2$ and are not accompanied by a large-scale low-speed event. Close to the wall, the roll modes induce the near-wall congregative motion. As time evolves, the flow response to these large-scale rolls is observed in the form of an amplifying negative-u perturbation. Based on the contour level, $u^+|_m = -1.0$, the width of the u response varies from 0.005 to 0.35. Therefore, there is a rapid growth and intensification of the negative-u field via the congregative motion induced by the large-scale circulation. In terms of the wall-normal extent, the solid contour in figure 16 initially reaches up to $y/\delta = 0.032$ ($y^+ = 30$). It subsequently expands and extends beyond $y/\delta = 0.3$, where the outer merging event takes place (see figure 15). Thus, the intense near-wall congregative motion induced by the outer large-scale circulation transforms into strong streamwise velocity fluctuations at the tail of the downstream structure. Because the local convection speed is proportional to the streamwise velocity fluctuations (Lee *et al.* 2014), the intense near-wall motions reduce the convection velocity of the downstream large-scale structure and, ultimately, lead to the merging event with the upstream structure.

The conditionally averaged velocity field at the reference streamwise location $r_x/\delta = 0$ is shown in figure 16(*b*). The negative-u structures, flanked on both sides by high-speed regions, have a width $\Delta z/\delta \simeq 0.4$ centred on the event location. Here, the centre of the in-plane circulation is at $y/\delta \simeq 0.15$ and $r_z/\delta \simeq \pm 0.25$, which is similar to the swirling patterns in figure 16(*a*). The scale of negative-u structures is enlarged in both the spanwise and the wall-normal directions. Simultaneously the adjoining large-scale circulations intensify and the near-wall vectors, which are parallel to the boundary, show larger spanwise velocity throughout the merging event. In addition, the large-scale circulation shows that the peripheral sweeps are followed by the opposing spanwise motions near the wall that probably enhance the negative u beneath the outer structures. The congregative motion and the increase in the negative u in the near-wall region thus accompany and facilitate the formation of the very long low-speed structures during the merging event.

4. Summary and conclusions

Conditional sampling of wall-bounded turbulent flows facilitates the study of the dynamics of turbulence structures, and in particular extracting specific events of interest within the flow field. By applying this technique to flow fields from DNS of turbulent channel flow at $Re_\tau = 930$, the spatial feature of long streaks associated with LSM and VLSM, and the accompanying near-wall behaviour, were investigated. Although the negative- and positive-u regions occupy similar area fractions within the flow field, their characteristics differ when divided into LSM (1–3δ) and VLSM ($>3\delta$). In the log layer, the positive LSM (1–3δ) occupy a larger area fraction than the negative counterpart. On the other hand, the very long positive-u regions ($>3\delta$) are less frequent than the negative ones. The area fractions are consistent with positive perturbations being generally shorter and wider than negative-u structures. Based on the conditional two-point correlation, both the footprints of the positive- and negative-u structures penetrate into the near-wall region. In addition, the magnitude and patterns of the correlations reveal that nVLSM and pLSM are the dominant structures in the log layer and are directly connected to the

https://doi.org/10.1017/jfm.2016.3 Published online by Cambridge University Press

near-wall region. The footprints associated with positive u are relatively wider than their negative counterpart. The different spanwise scale is due to the character of the near-wall perturbation field induced by the roll motions. The large-scale circulation associated with sweeps generates diverging wall jets in the spanwise direction, while the large-scale circulation associated with negative u has the form of ejections with near-wall opposing jets. These different spanwise near-wall motions of the positive and negative structures are parallelled by a difference in their contribution to near-wall Reynolds stresses.

The particular near-wall streaks that are connected to outer large-scale structures were conditionally sampled and their characteristics were analysed. The near-wall u under the footprints of positive LSMs are enhanced even in the viscous sublayer compared to the negative-u case. Also, the spanwise velocity fluctuations (w) are significantly modulated by positive-u LSMs, even more than u and v, which indicates that the large-scale positive-u events play a material role in the amplitude modulation of the near-wall small scales. The positive-u events also influence a relatively wider near-wall region by inducing the dispersive motion. On the other hand, the near-wall congregative motions of negative-u footprints contribute to the formation of very long negative-u regions ($>3\delta$) in the log layer. The congregation of near-wall streaks beneath the outer counter-rotating rolls generates intense velocity perturbations which are lifted away from the wall towards the outer large-scale structures. This process enhances the spatial coherence of the negative-u structures in the log layer. This same process was shown to take place during, and to partake into, the merging of negative large-scale perturbations to form VLSMs. The dynamics of merging of LSMs were examined using conditional averages with the condition being a merging event at $y/\delta = 0.15$. The results confirmed that the intense near-wall regions are a robust feature during the merging process, although further studies are needed in order to determine whether the generation of intense near-wall perturbations can be fully attributed to the congregation of near-wall streaks. Owing to the existence of large-scale circulations, the intense u regions are lifted up and evolve into the trailing edge of the downstream LSM. Since the convection velocity is slower around the strong u regions, the downstream LSM is retarded and merges with the upstream structure. As such, the formation of very long negative-u regions via merging events is directly related to the evolution of intense near-wall perturbations.

Our results demonstrate the different top-down influence of high- and low-speed large-scale structures, i.e. the dispersive and congregative motions associated with their respective outer large-scale circulations. Furthermore, the retardation of the outer low-speed structure was linked to the evolution of intense near-wall streamwise velocity fluctuations as part of a bottom-up process. The inner–outer interactions of negative-u structures lead to their locally different convection velocities. We also directly verify the dynamic role of the outer roll cell, which generates the intense near-wall motions, and ultimately facilitates merging of low-speed streaks into the very long low-speed regions that characterize the outer layer.

Acknowledgements

This work was supported by the Creative Research Initiatives (no. 2015-001828) programme of the National Research Foundation and was partially supported by KISTI under the Strategic Supercomputing Support Program.

Supplementary movies

Supplementary movies are available at http://dx.doi.org/10.1017/jfm.2016.3.

https://doi.org/10.1017/jfm.2016.3 Published online by Cambridge University Press

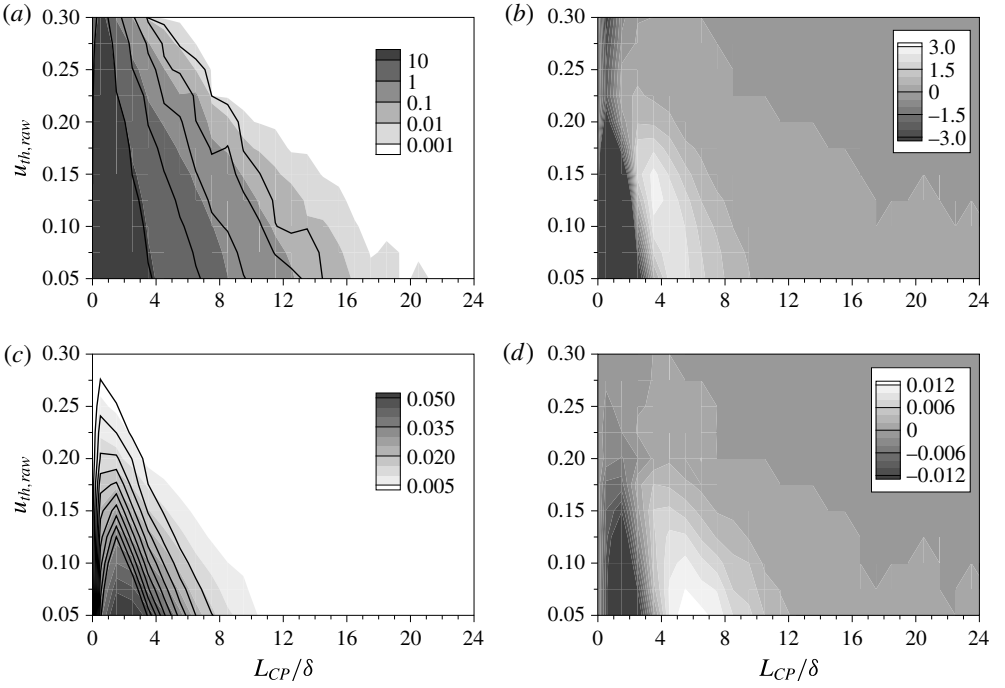


FIGURE 17. Histograms of the streamwise lengths (L_{CP}) of low- and high-speed streaks when using various velocity thresholds, $u_{th,raw}$. The bin size is $\Delta L_{CP} = 1\delta$. (*a*) The mean number of the streaks per field ($\langle N_{CP} \rangle$) in the wall-parallel plane. (*c*) The mean area occupied by the structures per field ($\langle \Pi_{CP} \rangle$) versus their streamwise lengths. (*a*,*c*) The flood and line contours represent low- and high-speed streaks, respectively. Difference in (*b*) mean number and (*d*) mean area between low- and high-speed regions; negative values indicate larger mean quantity for the high-speed streaks.

Appendix. Effect of the structure-identification threshold

To address the influence of the threshold value adopted in the structure identification, the populations and area fractions of the structures are re-evaluated over a range of thresholds from 0.05 to 0.3. The contour lines in figure 17(*a*) represent $\langle N_{CP} \rangle$ of the streaks as a function of the threshold level. When the magnitude of $u_{th,raw}$ is low, new contiguous regions are detected and previously detected regions combine to form longer structures. Thus the total number of the structures and number of those which reach the maximum length increase. However, the general trends do not change qualitatively, and the quantitative change in inappreciable. Regardless of the threshold value, the populations of the structures decrease logarithmically and the negative-u regions are longer than their positive counterparts. Figure 17(*b*) shows the difference in $\langle N_{CP} \rangle$ between the negative- and positive-u streaks. The darker grey contours indicate a lower $\langle N_{CP} \rangle$ for the negative-u streaks. The sign of the contours changes around 3δ independently of $u_{th,raw}$. Figure 17(*c*) shows the mean area $\langle \Pi_{CP} \rangle$ occupied by the streaks as a function of the threshold value. The peak remains between 1δ and 3δ independent of the threshold. The difference between the low- and high-speed regions is plotted in figure 17(*d*). Since the area fraction of the very long positive-u regions ($>3\delta$) drops rapidly compared to the negative ones for all values of $u_{th,raw}$, the sign of the contours changes at $L_{CP} = 3\delta$.

https://doi.org/10.1017/jfm.2016.3 Published online by Cambridge University Press

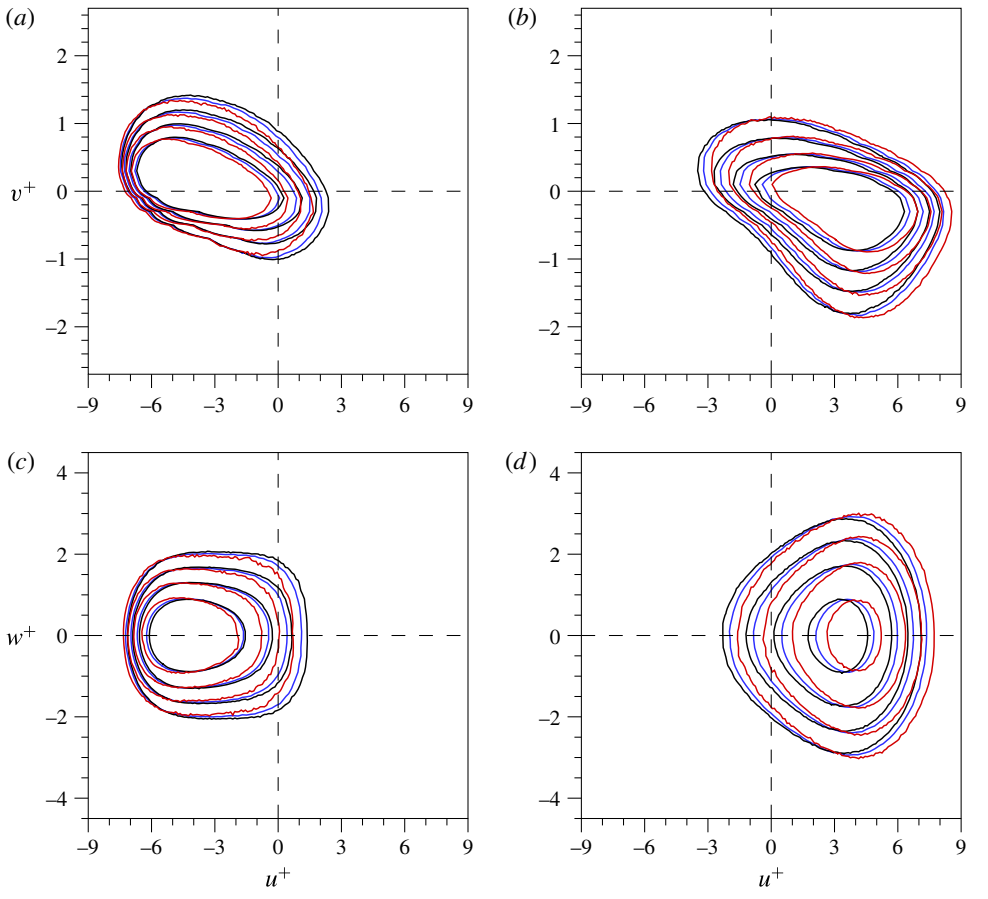


FIGURE 18. (Colour online) Joint p.d.f.s of (*a*,*b*) *u*–*v* and (*c*,*d*) *u*–*w* at $y^+ = 14.5$: (*a*,*c*) nVLSM and (*b*,*d*) pLSM. The threshold values are $u_{th,raw} = 0.05U_b$ (black), $0.1U_b$ (blue) and $0.2U_b$ (red). Contour levels are distributed exponentially from 0.005 to 0.05.

Figure 18 depicts the effect of three values of the threshold, $u_{th,raw} = 0.05$, 0.10, $0.20U_b$, on the joint p.d.f.s of *u*–*v* and *u*–*w* at $y^+ = 14.5$. The blue line is a reproduction of the results in figure 9. Although in figure 17 the total number of the detected regions depends on the threshold, the joint p.d.f.s collapse well regardless of $u_{th,raw}$. As the threshold value is doubled, the joint p.d.f.s shift very slightly to a higher magnitude of *u*. The shift is insignificant compared to the change in the threshold value because the present detection method extracts the long *u* regions based on the local maxima in the field. The asymmetry between the distributions of positive- and negative-*u* events in figure 9 persists independently of the threshold for the same reason.

REFERENCES

ADRIAN, R. J. 2007 Hairpin vortex organization in wall turbulence. *Phys. Fluids* **19** (4), 041301.

ADRIAN, R. J., MEINHART, C. D. & TOMKINS, C. D. 2000 Vortex organization in the outer region of the turbulent boundary layer. *J. Fluid Mech.* **422**, 1–54.

https://doi.org/10.1017/jfm.2016.3 Published online by Cambridge University Press

AGOSTINI, L. & LESCHZINER, M. A. 2014 On the influence of outer large-scale structures on near-wall turbulence in channel flow. *Phys. Fluids* **26** (7), 075107.

AHN, J., LEE, J. H., LEE, J., KANG, J.-H & SUNG, H. J. 2015 Direct numerical simulation of a 30R long turbulent pipe flow at $Re_\tau = 3008$. *Phys. Fluids* **27** (6), 065110.

DEL ÁLAMO, J. C. & JIMÉNEZ, J. 2003 Spectra of the very large anisotropic scales in turbulent channels. *Phys. Fluids* **15** (6), L41.

DEL ÁLAMO, J. C. & JIMÉNEZ, J. 2006 Linear energy amplification in turbulent channels. *J. Fluid Mech.* **559**, 205–213.

BALAKUMAR, B. J. & ADRIAN, R. J. 2007 Large- and very-large-scale motions in channel and boundary-layer flows. *Phil. Trans. R. Soc. Lond.* A **365** (1852), 665–681.

BALTZER, J. R., ADRIAN, R. J. & WU, X. 2013 Structural organization of large and very large scales in turbulent pipe flow simulation. *J. Fluid Mech.* **720**, 236–279.

CHUNG, D. & MCKEON, B. J. 2010 Large-eddy simulation of large-scale structures in long channel flow. *J. Fluid Mech.* **661**, 341–364.

DENNIS, D. J. C. & NICKELS, T. B. 2011 Experimental measurement of large-scale three-dimensional structures in a turbulent boundary layer. Part 2. Long structures. *J. Fluid Mech.* **673**, 218–244.

GANAPATHISUBRAMANI, B. 2008 Statistical structure of momentum sources and sinks in the outer region of a turbulent boundary layer. *J. Fluid Mech.* **606**, 225–237.

GANAPATHISUBRAMANI, B., HUTCHINS, N., MONTY, J. P., CHUNG, D. & MARUSIC, I. 2012 Amplitude and frequency modulation in wall turbulence. *J. Fluid Mech.* **712**, 61–91.

GANAPATHISUBRAMANI, B., LONGMIRE, E. K. & MARUSIC, I. 2003 Characteristics of vortex packets in turbulent boundary layers. *J. Fluid Mech.* **478**, 35–46.

GUALA, M., HOMMEMA, S. E. & ADRIAN, R. J. 2006 Large-scale and very-large-scale motions in turbulent pipe flow. *J. Fluid Mech.* **554**, 521–542.

HOYAS, S. & JIMÉNEZ, J. 2006 Scaling of the velocity fluctuations in turbulent channels up to $Re_\tau = 2003$. *Phys. Fluids* **18** (1), 011702.

HUTCHINS, N. & MARUSIC, I. 2007*a* Evidence of very long meandering features in the logarithmic region of turbulent boundary layers. *J. Fluid Mech.* **579**, 1–28.

HUTCHINS, N. & MARUSIC, I. 2007*b* Large-scale influences in near-wall turbulence. *Phil. Trans. R. Soc. Lond.* A **365** (1852), 647–664.

HWANG, Y. & COSSU, C. 2010 Self-sustained process at large scales in turbulent channel flow. *Phys. Rev. Lett.* **105** (4), 044505.

KIM, K., BAEK, S. J. & SUNG, H. J. 2002 An implicit velocity decoupling procedure for the incompressible Navier–Stokes equations. *Intl J. Numer. Meth. Fluids* **38** (2), 125–138.

KIM, K. C. & ADRIAN, R. J. 1999 Very large-scale motion in the outer layer. *Phys. Fluids* **11** (2), 417–422.

LEE, J., AHN, J. & SUNG, H. J. 2015 Comparison of large- and very-large-scale motions in turbulent pipe and channel flows. *Phys. Fluids* **27** (2), 025101.

LEE, J., LEE, J. H., CHOI, J.-I. & SUNG, H. J. 2014 Spatial organization of large-and very-large-scale motions in a turbulent channel flow. *J. Fluid Mech.* **749**, 818–840.

LEE, J. H. & SUNG, H. J. 2011 Very-large-scale motions in a turbulent boundary layer. *J. Fluid Mech.* **673**, 80–120.

LEE, J. H. & SUNG, H. J. 2013 Comparison of very-large-scale motions of turbulent pipe and boundary layer simulations. *Phys. Fluids* **25** (4), 045103.

LIU, Z., ADRIAN, R. J. & HANRATTY, T. J. 2001 Large-scale modes of turbulent channel flow: transport and structure. *J. Fluid Mech.* **448**, 53–80.

MATHIS, R., HUTCHINS, N. & MARUSIC, I. 2009 Large-scale amplitude modulation of the small-scale structures in turbulent boundary layers. *J. Fluid Mech.* **628**, 311–337.

MCKEON, B. J. & SHARMA, A. S. 2010 A critical-layer framework for turbulent pipe flow. *J. Fluid Mech.* **658**, 336–382.

MITO, Y., HANRATTY, T. J., ZANDONADE, P. & MOSER, R. D. 2007 Flow visualization of superbursts and of the log-layer in a DNS at $Re_\tau = 950$. *Flow Turbul. Combust.* **79** (2), 175–189.

MONTY, J. P., HUTCHINS, N., NG, H. C. H., MARUSIC, I. & CHONG, M. S. 2009 A comparison of turbulent pipe, channel and boundary layer flows. *J. Fluid Mech.* **632**, 431–442.

https://doi.org/10.1017/jfm.2016.3 Published online by Cambridge University Press

MONTY, J. P., STEWART, J. A., WILLIAMS, R. C. & CHONG, M. S. 2007 Large-scale features in turbulent pipe and channel flows. *J. Fluid Mech.* **589**, 147–156.

NOLAN, K. P. & ZAKI, T. A. 2013 Conditional sampling of transitional boundary layers in pressure gradients. *J. Fluid Mech.* **728**, 306–339.

SILLERO, J. A., JIMÉNEZ, J. & MOSER, R. D. 2014 Two-point statistics for turbulent boundary layers and channels at Reynolds numbers up to $\delta^+ = 2000$. *Phys. Fluids* **26** (10), 105109.

TALLURU, K. M., BAIDYA, R., HUTCHINS, N. & MARUSIC, I. 2014 Amplitude modulation of all three velocity components in turbulent boundary layers. *J. Fluid Mech.* **746**, R1.

TOH, S. & ITANO, T. 2005 Interaction between a large-scale structure and near-wall structures in channel flow. *J. Fluid Mech.* **524**, 249–262.

TOMKINS, C. D. & ADRIAN, R. J. 2003 Spanwise structure and scale growth in turbulent boundary layers. *J. Fluid Mech.* **490**, 37–74.

WALLACE, J. M., ECKELMANN, H. & BRODKEY, R. S. 1972 The wall region in turbulent shear flow. *J. Fluid Mech.* **54** (01), 39–48.

WU, X., BALTZER, J. R. & ADRIAN, R. J. 2012 Direct numerical simulation of a $30R$ long turbulent pipe flow at $R^+ = 685$: large- and very large-scale motions. *J. Fluid Mech.* **698**, 235–281.

ZAKI, T. A. 2013 From streaks to spots and on to turbulence: exploring the dynamics of boundary layer transition. *Flow Turbul. Combust.* **91** (3), 451–473.

ZHOU, J., ADRIAN, R. J., BALACHANDAR, S. & KENDALL, T. M. 1999 Mechanisms for generating coherent packets of hairpin vortices in channel flow. *J. Fluid Mech.* **387**, 353–396.

https://doi.org/10.1017/jfm.2016.3 Published online by Cambridge University Press